

5-2016

Investigation of Pin Fin Cooling Channels for Applications in Gas Turbines

Royce Fernandes

Follow this and additional works at: <https://commons.erau.edu/edt>



Part of the [Aerospace Engineering Commons](#)

Scholarly Commons Citation

Fernandes, Royce, "Investigation of Pin Fin Cooling Channels for Applications in Gas Turbines" (2016).
Dissertations and Theses. 210.
<https://commons.erau.edu/edt/210>

This Thesis - Open Access is brought to you for free and open access by Scholarly Commons. It has been accepted for inclusion in Dissertations and Theses by an authorized administrator of Scholarly Commons. For more information, please contact commons@erau.edu.

INVESTIGATION OF PIN FIN COOLING CHANNELS FOR APPLICATIONS IN
GAS TURBINES

A Thesis
Submitted to the Faculty of
Embry-Riddle Aeronautical University

By

Royce Fernandes

In Partial Fulfillment of the
Requirements for the Degree of
Master of Science in Aerospace Engineering

May 2016
Embry-Riddle Aeronautical University
Daytona Beach, Florida

INVESTIGATION OF PIN FIN COOLING CHANNELS FOR APPLICATIONS IN
GAS TURBINES

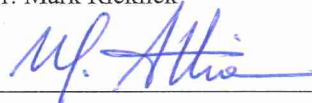
By

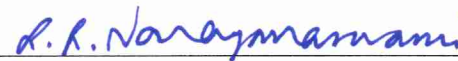
Royce Fernandes


A Thesis prepared under the direction of the candidate's committee chairman, Dr. Mark Ricklick, Department of Aerospace Engineering, and has been approved by the members of the thesis committee. It was submitted to the School of Graduate Studies and Research and was accepted in partial fulfillment of the requirements for the degree of Master of Science in Aerospace Engineering.

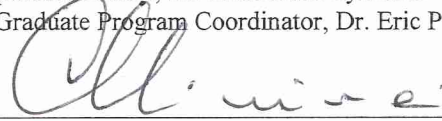
THESIS COMMITTEE

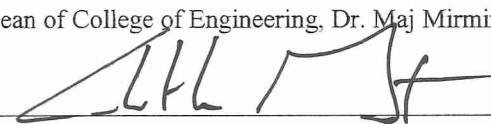

Chairman, Dr. Mark Ricklick


Member, Dr. Magdy Attia


Member, Dr. Laksh Narayanaswami


Department Chair, Dr. Anastasios Lyrintzis
or Graduate Program Coordinator, Dr. Eric Perrell


Dean of College of Engineering, Dr. Maj Mirmirani


Vice Chancellor, Academic Support, Dr. Christopher Grant

21 April 2016
Date

4/21/16
Date

4/25/16
Date

ACKNOWLEDGMENTS

I would like to dedicate this work to my family who have supported and encouraged me to follow my interest whole heartedly without any compromise, whatever be the situation. A special thanks to my advisor Dr. Mark Ricklick, for the patience, guidance, support, and the fun boat trips that added to the learning and research experience. Without your instruction, guidance and motivation the completion of this project wouldn't be possible. It's truly been an honor having you as my advisor.

I would also like to extend my gratitude to my committee members Dr. Narayanaswami and Dr. Attia who have guided me not only with my thesis, but who have also been great teachers throughout the course of my studies as an undergrad and graduate student. The engine design classes I have taken with them have truly been some of the most interesting and informative classes. I would also like to thank all my professors at ERAU for preparing me for the industry and my life ahead and teaching me to always dream big. This study was also supported by an internal research grant for which I would like to thank the Department of Aerospace Engineering for letting me be a part of their distinguished team of research professionals.

Finally, a special thanks to my lab mates Bhushan Upalkar, Yash Mehta and Yogesh Pai who played a vital role in helping to start and set-up the Propulsion Thermal Management Lab at ERAU. Thanks to all the friends I have met here at ERAU throughout my engineering course. Without their support, parties and the overall fun times none of this would have been possible.

TABLE OF CONTENTS

LIST OF FIGURES	vi
SYMBOLS.....	ix
ABBREVIATIONS	x
ABSTRACT.....	xi
1. Introduction	1
1.1. Motivation.....	1
1.2. Thermodynamics	2
1.3. Turbine Blade Cooling.....	3
1.4. Pin Fin Channel.....	6
1.5. Objective.....	8
2. Literature Review	10
2.1. Turbine blade cooling.....	10
2.2. Pin Fin cooling.....	10
2.3. Biomimicry Cooling Channel	19
3. Pin Fin Channel Benchmarking Study	23
3.1. Pin Fin Computational Set-up	23
3.1.1. Mesh/Grid Studies	25
3.1.2. Turbulence Models Investigated.	27
3.1.3. Data Reduction	28
3.2. Pin Fin Benchmarking Results and Analysis.....	28
3.2.1. Row 1 Heat Transfer Data	31
3.2.2. Row 5 Heat Transfer Data.....	35
3.2.3. Row 5 Pressure Data	39
4. Biomimicry Channel: Seal Whisker Pin	42
4.1. Biomimicry Channel Computational Set-up	42
4.2. Biomimicry Channel Results and Analysis	44
4.2.1. Biomimicry Channel Heat Transfer Data	46
4.2.2. Biomimicry Channel Pressure Data	48
5. Pin Fin Channel Experiment	49
5.1. Experimental Set-up.....	49
5.1.1. Experimental Rig Design	49
5.1.2. Data Reduction.....	52
5.2. Experimental Data and Analysis	52
6. Conclusion.....	62
7. Recommendations	63
8. Publications Resulting from Current Study.....	64

REFERENCES	65
------------------	----

LIST OF FIGURES

Figure 1-1: Brayton Cycle	2
Figure 1-1-2: Turbine inlet temperatures over the years (Wadley Research Group, 2013)	4
Figure 1-3: Blade cooling techniques (Han, 2004)	5
Figure 1-4: CFD simulation of flow features in a pin fin channel.....	6
Figure 2-1: Cross-section of pin fins (Sahiti et al., 2006).....	12
Figure 2-2: Pin fin array Nu as a function of Re (Sahiti et al., 2006).....	13
Figure 2-3: Pin fin array Eu as a function of Re (Sahiti et al., 2006).....	13
Figure 2-4: Wedge ducts of different orientation of outlet flow (Hwang & Lui, 2002).....	14
Figure 2-5: Friction factor as a function of Reynolds number (Peles et al., 2005).....	15
Figure 2-6: End wall Nu distributions for test channels with (a) attached pin-fins (b) detached pin-fins of $C/d = 1/4$, (c) detached pin-fins of $C/d = 2/4$ and (d) detached pin-fins of $C/d = 3/4$ at $Re = 30,000$. (Chang et al., 2008).....	17
Figure 2-7: Variation of friction factor with Re (Chang et al., 2008).....	18
Figure 2-8: Scans of Pinniped vibrissae using optical microscope showing vibrissae parameters (Shyam et al., 2015).....	19
Figure 2-9: Blades geometries simulated in CFD (Shyam et al., 2015).....	20
Figure 2-10: Incidence tolerance - Comparison between baseline VSPT blade and S1R0P5 over a wide range of incidence angles (-37° , 0° , 5° and 10°) (Shyam et al., 2015).....	21
Figure 2-11: Numerical simulation of the wake-flow behind different cylinder bodies (Hanke et al., 2010).....	22
Figure 3-1: Internal heat transfer and flow facility showing staggered pin fin array test section (Ames et al., 2006).....	23
Figure 3-2: Pin fin computational domain.....	24

Figure 3-3: Mesh refinement study.....	26
Figure 3-4: Isometric view of the final mesh.....	26
Figure 3-5: Close-up view of the mesh.....	26
Figure 3-6: Row-by-row Nusselt Number Comparison.....	29
Figure 3-7: Turbulent dissipation rate $Re = 30,000$	30
Figure 3-8: Row 1 Circumferential $Nu/Re^{1/2}$ comparison $Re = 3,000$	31
Figure 3-9: Row 1 Circumferential $Nu/Re^{1/2}$ comparison $Re = 10,000$	32
Figure 3-10: Row 1 Circumferential $Nu/Re^{1/2}$ comparison $Re = 30,000$	33
Figure 3-11: Comparison of mid-plane Mach number contours $Re = 3,000$	34
Figure 3-12: Row 5 Circumferential $Nu/Re^{1/2}$ comparison $Re = 3,000$	35
Figure 3-13: Row 5 Circumferential $Nu/Re^{1/2}$ comparison $Re = 10,000$	36
Figure 3-14: Row 5 Circumferential $Nu/Re^{1/2}$ comparison $Re = 30,000$	37
Figure 3-15: Circumferential C_p comparison $Re = 3,000$	39
Figure 3-16: Circumferential C_p comparison $Re = 30,000$	39
Figure 4-1: Bio Pin geometries used for the study	42
Figure 4-2: Elliptical bio pin computational domain	43
Figure 4-3: Polyhedral mesh with well-defined boundary layer	44
Figure 4-4: Elliptic bio pin front and side view	45
Figure 4-5: Circumferential Nu comparison $Re = 5,000$	46
Figure 4-6: Row-by-row Pin Nusselt Number Comparison	47
Figure 4-7: Pressure profile across the channel.....	48
Figure 5-1: Rig Geometry	49
Figure 5-2: Experimental Rig Set-up	50
Figure 5-3: TSP calibration curve.....	51
Figure 5-4: Heat leak with increase in temperature	52
Figure 5-5: Experimental Nusselt number contour	54
Figure 5-6: Smooth Channel Nusselt number plot	54

Figure 5-7: Nusselt number contour on experimental test section end wall	55
Figure 5-8: Nusselt number contour $Re = 10,000$ A] Heat flux = 450 W/m^2 B] Heat flux = 1200 W/m^2	56
Figure 5-9: Spanwise average Nusselt number $Re = 10,000$	57
Figure 5-10: Nusselt number contour $Re = 15,000$ A] Heat flux = 1300 W/m^2 B] Heat flux = 3200 W/m^2	58
Figure 5-11: Spanwise average of Nusselt number $Re = 15,000$	58
Figure 5-12: Nu Profiles for pin fin channels with $C/d = 0, 1/4, 2/4$, and $3/4$ at $Re = 30,000$ (Chang et al., 2008).....	60
Figure 5-13: Pressure drop across the channel at different Reynolds Numbers.....	61
Figure 7-1: Cylindrical bio pin channel velocity contour	63

SYMBOLS

ε	Turbulent Dissipation Rate (Tdr) or Strain Energy
η	Efficiency
ϖ	Strain Energy per unit volume
D	Hydraulic Diameter
f	Friction Factor
H	Heat transfer coefficient
I	Intensity of the paint
I_r	Reference Image Intensity of the paint
k_{air}	Thermal Conductivity of Air
k_I	Thermal Conductivity of Inconel
K	Turbulent kinetic energy (Tke)
M	Mach Number
\dot{M}	Mass flow rate
Nu	Nusselt Number
Pr	Prandtl Number
P_s	Static Pressure
P_0	Total Pressure
Re	Reynolds Number
Sc	Schmidt Number
T	Temperature
T_3	Turbine Inlet Temperature
T_4	Turbine Exhaust Temperature
T_w	Temperature of the wall
Tr	Reference Temperature of the fluid
x	Distance in Stream wise direction
X/D	Stream wise distance in terms of hydraulic diameter

ABBREVIATIONS

CFD	Computational Fluid Dynamics
CAD	Computer Aided Design
RANS	Reynolds Averaged Navier Stokes
LES	Large Eddy Simulation
DNS	Direct Numerical Solution
BR	Blowing Ratio
EB	Elliptic Blending
STAR-CCM+	Simulation of Turbulence in Arbitrary Regions-Computational Continuum Modeling
CCD	Charge Coupled Device
TSP	Temperature Sensitive Paint
PSP	Pressure Sensitive Paint
LED	Light Emitting Diodes
DB	Dittus-Boelter

ABSTRACT

Researcher: Royce Fernandes

Title: Investigation of Pin Fin Cooling Channels for Applications in Gas Turbines

Institution: Embry-Riddle Aeronautical University

Degree: Master of Science in Aerospace Engineering

Year: 2016

Gas turbine blades are often cooled using internal cooling channels to prevent failure at temperatures beyond material limitations. Pin fin channels are commonly used on the trailing edge of the blades, where they enhance heat transfer and also provide structural support. This study focuses on the validation of several commercially available RANS turbulence models in CFD, that are used to computationally simulate the flow features inside a pin fin cooling channel. Turbulence models investigated are: Menter's $k-\omega$ SST, realizable $k-\epsilon$, and a quadratic formulation of the realizable $k-\epsilon$ model. The geometry investigated is a staggered 8 row pin fin channel. Results have shown that depending on the location in the channel and Reynolds number, the QRK-E and KO-SST models produce superior matching of heat transfer coefficients to experimental data. Comparisons have also shown that depending on Reynolds number, the RK-E and QRK-E models match pressure coefficient data the closest.

An investigation of a biomimicry pin channel created using the undulations observed on seal whiskers also showed improvements in heat transfer levels and reduced pressure drops across the channel. The undulation treatment was applied to an elliptical and cylindrical pin. Preliminary results have shown that the cylindrical bio pins showed an increase in heat transfer levels with a significant reduction in pressure losses in the channel.

1. Introduction

1.1 Motivation

Energy requirements for power generation have always been steadily increasing over the last few decades. Utilizing minimum amounts of energy while maximizing efficiency and power output is one of the major criteria's for today's engine manufacturers. Gas turbines are often used as a means of power generation because of their high efficiency and large power to weight ratios. They are used for power generation in land, sea and air based systems. Since its introduction, the efficiency of gas turbine engines has continuously risen. Thermal energy from combustion is converted into work which is used to satisfy everyday power requirements. The Brayton cycle governs the working of a gas turbine engine. Air is first compressed followed by the addition of heat, which is then converted into work extracted by the turbine blades. The temperature reaches its highest level at turbine entry, and the maximum allowable temperature there is limited by the material used in its construction.

The efficiency of gas turbine engines increases with the increase in turbine inlet temperatures. At operating conditions the temperatures inside the power plant ranges from 1600° C to 2100° C (Han et al., 2012). Over the last few decades, advances in material technology and improvements in the understanding of aerodynamics and combustion have contributed to the increased efficiency and success of gas turbine engines. High performance materials like special steels, titanium alloys and super alloys are often used in the construction of gas turbines. However, even the sophisticated alloys used for making turbine blades have melting points below engine operating temperatures. As engine operation temperatures increased, blades needed to be cooled to prevent them from melting

and to avoid failure during operation. This is typically accomplished by using bleed air from the compressor section of the engine. High turbine inlet temperatures are possible only with advanced blade cooling techniques. Advances in component cooling technology have played the biggest role in improving the performance and efficiency of turbine engines.

The work described in this thesis involved the investigation of advanced blade cooling channels. Specifically, the study focuses on pin fin internal cooling channels in turbine blades. The flow features and obstructions in an internal pin fin cooling channel enhance and promote heat transfer on the blade surface. Internal cooling channels with advanced geometries using biomimicry concepts are also looked into.

1.2 Thermodynamics

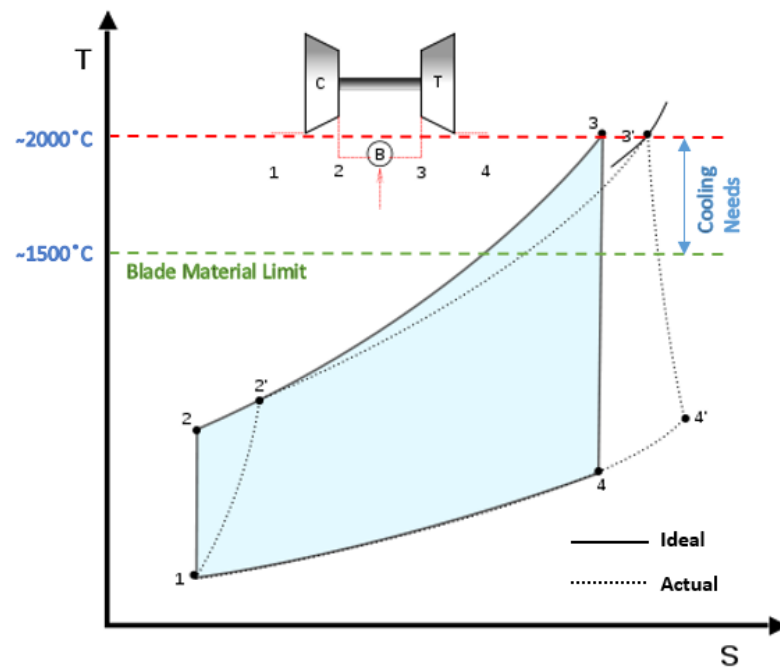


Figure 1-1: Brayton Cycle

The working of the gas turbine engine is governed by the processes of the Bryton cycle shown in Figure 1-1. The compressor section of the engine pressurizes the air entering the engine. This is followed by the addition of heat in the combustor by igniting the fuel-air mixture. This causes the energized air to expand in the turbine section of the engine with a high velocity. The turbine blades extract the energy from this high velocity energized flow exiting the combustor.

The equation that governs the efficiency of the Brayton cycle is given by:

$$\eta = 1 - \frac{T_4}{T_3} \quad (1)$$

T_3 represent the turbine inlet temperature, which is the temperature of the high velocity hot fuel-air mixture exiting the combustor. The above equation demonstrates what has been alluded to before that as T_3 increases the efficiency of the Brayton cycle increases. Therefore, engine manufacturers strive to achieve the highest turbine inlet temperatures within the safe operating limits of the blade materials.

1.3 Turbine Blade Cooling

Over the past few decades advances in material technology and manufacturing have made it possible to create nickel based super alloys that are capable of withstanding very high temperatures with melting points close to 1500° C. Thermal barrier coating on the blades have also allowed for higher operating temperatures. Figure 1-2 shows the improvements in blade material and cooling technology that have allowed for higher turbine inlet temperatures over the last few decades. The figure shows that manufacturers started to look into and use turbine blade cooling techniques in the 1980's, first starting

with external cooling techniques like film cooling. In the last two decades, with an improved understanding of blade cooling and increased engine operation temperatures, manufacturers started to look at internal blade cooling concepts. Experimental and CFD analysis was used to study complex internal cooling geometries that provided for high heat transfer rates. The last few years have also seen the use of ceramic matrix composites to manufacture turbine blades. What's innovative about CMC is that it can be made as strong as metal, yet much lighter and can withstand much higher temperatures (GE Global Research).

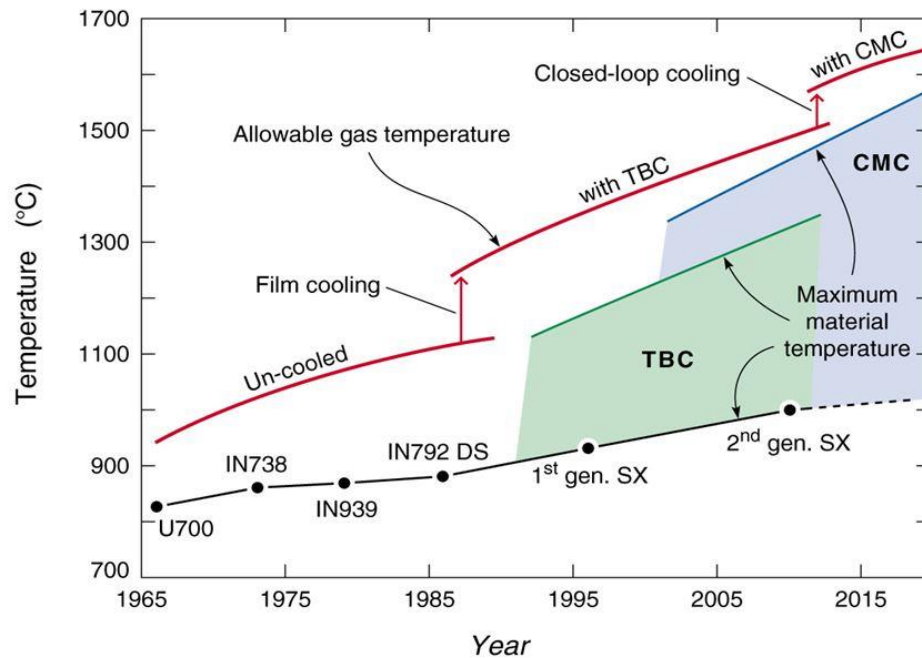


Figure 1-2: Turbine inlet temperatures over the years (Wadley Research Group, 2013)

The maximum attainable temperatures ultimately depend on the maximum combustion temperature of the fuels used for power generation today, which can reach temperatures close to 2000° C (Meher-Homji et al., 2010). To bridge the gap between the maximum allowable temperature limit of today's sophisticated alloys (1500° C) and the

maximum attainable fuel combustion temperatures (2000°C), modern cooling techniques need to be adopted to prevent component failure. Modern gas turbine engines use innovative internal and external cooling techniques to cool down the turbine blades and prevent material failure at very high temperature operating conditions. Improvements in cooling techniques will permit turbine operations ever closer to the maximum allowable combustion temperature.

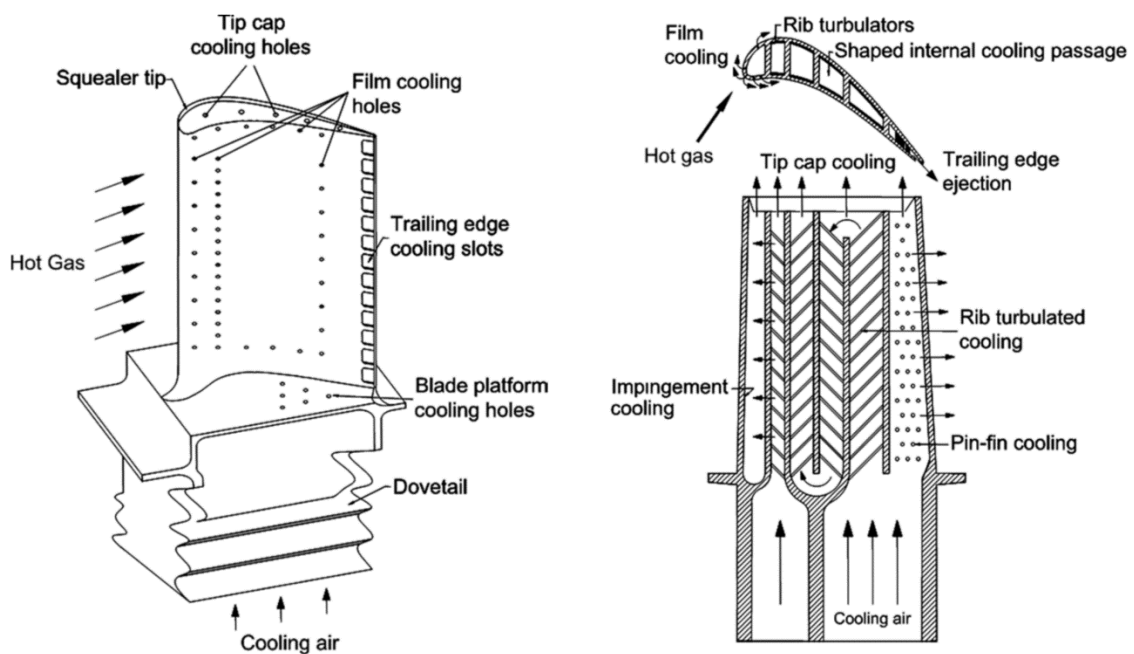


Figure 1-3: Blade cooling techniques (Han, 2004)

Figure 1-3 shows some of the blade cooling techniques used in the industry today. External cooling uses bleed air from the compressors to form a film of cool air over the external blade surface thereby protecting it from the hot gasses exiting the combustor. Hollow blades with internal cooling channels with various features are also used to enhance heat transfer from within the blade. Some of the internal cooling techniques use impingement channels, rib turbulated channels and pin fin channels to cool the turbine blades. These channels are located at different locations within the blade depending on the

amount of heat transfer required. Impingement channels are often used on the leading edge of the blade. Here, the coolant impinges on the hot surface, creating a stagnation point flow that enhances heat transfer. Rib turbulated channels are used in the mid-section of the blade. The ribs in the flow channel create re-circulating flow zones that promote shear stresses and flow mixing that increase levels of heat transfer. Pin fin channels are often used on the trailing edge of the blade where they also serve an additional purpose of providing structural support. Pin Fin channels increase the internal surface area of the blade and also act as obstructions that create turbulent flows which act as drivers of heat transfer. This study focuses on internal pin fin channels used to enhance heat transfer in turbine blades.

1.4 Pin Fin Channel

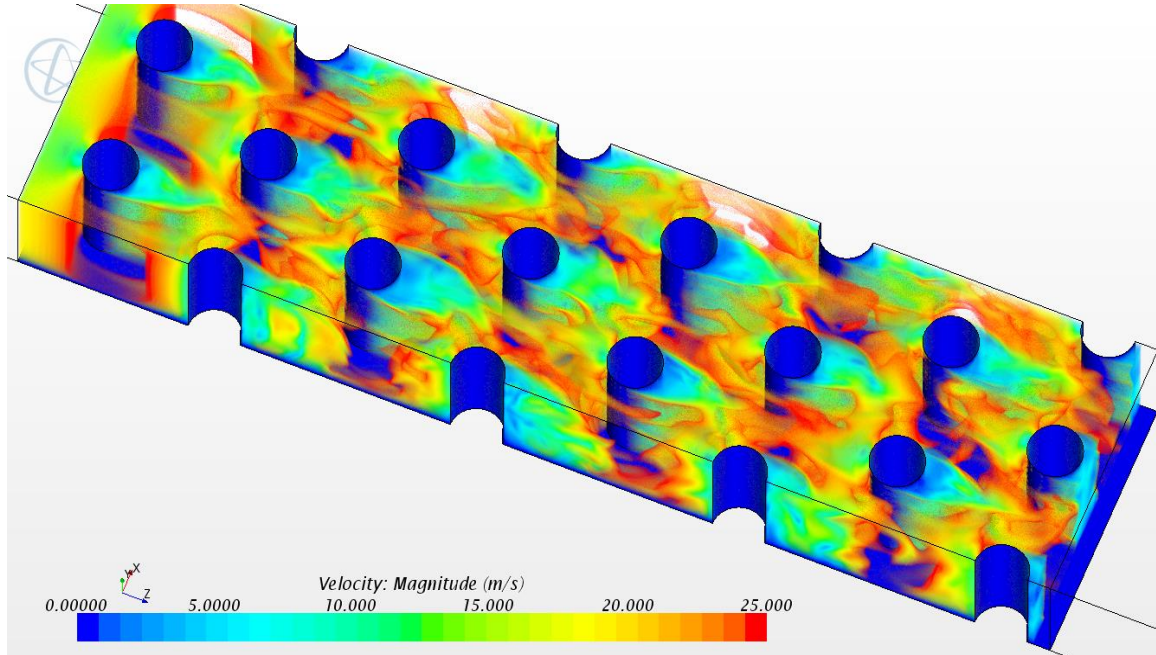


Figure 1-4: CFD simulation of flow features in a pin fin channel

Figure 1-4 represent a typical pin fin channel geometry, highlighting some of the flow features involved. A pin fin channel is made up of an array of fins, usually cylindrical fins, arranged in an in-line pattern, staggered pattern or any other pattern as desired. An ideal pin fin channel contains 7-8 rows of pins. An internal cooling channel with a pin fin array is characterized by regions of accelerated flows in between the pins, stagnation flows, localized low and high pressure regions, flow separation zones and end wall boundary layer flow features that enhance the rates of convective heat transfer (Ames, Chyu, Han, Metzger). In a pin fin channel flow stagnates on the front surface of the pin and then accelerates around it before separating. The resulting shedding caused by unsteady separation is a significant driver of heat transfer on the backside of the pin (Ames, Dvorak, 2006). Particular areas of interest for the current study include the leading edge region and the trailing edge wake region. The flow features in these regions provide for high heat transfer rates from the pin surface. The presence of a cylinder in the flow channel also breaks up the boundary layer on the end walls due to the formation of a flow commonly referred to as a horseshoe vortex. This horseshoe vortex produces high wall shear stresses beneath it, resulting in high heat transfer from the end wall in this region (Chyu et al., 1999).

Pin fin channels are known to perform effectively. Previous studies have shown that the flow physics associated with the heat transfer performance of the pin and enwalls results in higher levels of heat transfer on the pin surface by 35% (VanFossen, 1982) and 10-20% on the end walls (Chyu et al., 1999). Compared to smooth channels, pin fin channels experience an adverse pressure gradient caused by the flow disturbances. In a pin fin array the flow around the pin causes turbulent wakes, which increase as the flow moves

downstream. These turbulent wakes result in high levels of total pressure loss in these regions.

1.5 Objectives

Several groups conducted experimental analysis on pin fin channels of various geometries and configurations. In recent years the use of computational fluid dynamics (CFD) to solve and analyze fluid flows had increased and is being used widely in the industry. CFD uses the Reynolds Averaged Navier-Stokes equations to solve and predict fluid flow properties. Variations of these equations in the latest CFD turbulence models account for most of the fluid flow properties. However, with no definitive and complete solution to defining and understanding the phenomenon of turbulence in nature, CFD numerical models come with a certain degree of inaccuracy.

For purposes of optimization, experimental analysis is time consuming and expensive. The need for accurate CFD predictions is aimed at the industrial need for more cost effective testing models. The objectives of the study are listed below.

1. The first objective involved examining the accuracy of some of the available turbulence models for heat transfer and pin surface pressure distribution. Determining the accuracy of the turbulence models for predicting heat transfer and pressure profiles around the pin was achieved by benchmarking a computational geometry and comparing the data against data obtained from an experimental setup available in the literature.
2. The second objective involved studying highly advanced geometries to improve upon the levels of heat transfer and to reduce the pressure drop in the channel. This involved using biomimicry (imitating nature in

engineering) features to enhance channel performance. Although pin fins perform effectively to enhance heat transfer in cooling channels, they cause an undesirable pressure drop across the channel. The adverse pressure gradients created by the flow around a cylinder at the stagnation region and wake region cause a total pressure drop across the channel. Manufacturers strive to achieve the lowest pressure drops across the channels especially in turbine sections of engines in order to maintain engine efficiency. The undulations (peaks and valleys) in seal whiskers was studied and implemented on to the pin fins. Studies have shown that the undulations on the surface reduce drag considerably. The effect of the undulations on channel performance was studied to make improvements over the standard pin fins.

3. The third objective involved designing, building and setting up an experimental facility to study the end wall and pin heat transfer together, since most research groups studied either end wall or pin fin heat transfer separately.

2. Literature Review

2.1 Turbine Blade Cooling

Developments in gas turbine cooling technology have played a crucial role in increasing engine efficiency and power output. Gas turbine engines often operate at temperatures close to 2000° C. The operating temperatures are often far above the permissible metal temperatures. The airfoil section in turbine blades must be able to sustain thermal and mechanical stresses, fatigue, creep and chemical deterioration while maintaining an acceptable operating life (Morris, 1996). For safe operation turbine blades need to be cooled. The blades are cooled using bleed air from the compressor section of the engine.

The cooling system for the blades must be designed so as to ensure that the maximum surface temperatures are within the allowable thermal stress limits to maintain durability and component life. Too little coolant flow results in hotter blade temperatures and reduced component life. Similarly, too much coolant flows result in reduced engine performance (Ekkad et al., 2012). As previously discussed some of the advanced cooling techniques used today include film cooling, impingement cooling, rib turbulated and pin fin channel cooling.

2.2 Pin Fin Cooling Channel

From the early days of convective cooling channels in turbine blades, studies have been done on various types of channels to enhance heat transfer while maintaining a low pressure drop and minimum mass flow rate. Studies have shown that the behavior of the

flow around a cylinder significantly impacts the levels of heat transfer from the cylinder surface and end wall (Ricklick, 2014). To determine the effectiveness of the pin fin channel, experiments have been conducted to study the effects of pin arrangement in the array, the effects of pin height and diameter on the heat transfer coefficient and the effect of the number of rows of pins in the array.

Ames et al., (2006) experimentally investigated the fluid dynamics of a pin fin array in order to clarify the physics of heat transfer and uncover problems in conventional turbulence models. They studied the fluid dynamics of a staggered pin fin array using hot wire anemometry at array Reynolds numbers of 3,000, 10,000 and 30,000. The study acquired pin mid line surface pressure distributions and pin midline heat transfer distributions. The results of the study concluded that the flow was significantly unsteady due to shedding of pins. The intensity of the shedding increased with increase in Reynolds number. Near-pin span wise velocity distributions showed evidence of separation in the first two rows. Subsequent rows showed very high near-wall turbulence levels, providing evidence of unsteady separation. A CFD benchmarking study showed the turbulence models used under predicted heat transfer and pressure drop through the array.

An experimental analysis conducted by Brigham and VanFossen (1984) studied the heat transfer from short pin fins which indicated lower levels of heat transfer when compared to longer pins with the same configuration. Two sets of experiments were run, both with a four row staggered array set of pins. One array had pins 2-dia long spaced 4-dia apart and the other had pins $\frac{1}{2}$ -dia long spaced 2-dia apart. Array averaged heat transfer for these two sets were found to be considerably lower than arrays containing more rows of longer pins. The study concluded that the pin diameter ratio is the dominant factor in the

level of heat transfer coefficients for short pins. The number of streamwise rows had a slight effect on heat transfer, with heat transfer coefficients increasing with the addition of rows in the streamwise direction. For an L/D less than 2, the Nusselt number is a function of Reynolds Number.

Experimental studies have shown that although the cylindrical pin fin geometry shows higher heat transfer compared to other geometries and configurations, the high pressure drop that accompanies these pins reduces their overall performance substantially. Sahiti et al. (2006) numerically investigated six different pin cross sections to study its influence on pressure drop and heat transfer capabilities. Figure 2-1 shows the six different cross sections studied, which included a NACA airfoil, dropform, lancet, elliptic, circular and square cross section.

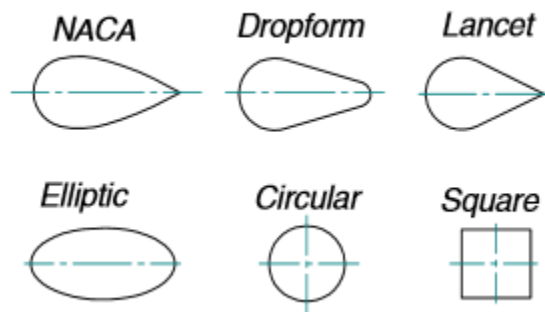


Figure 2-1: Cross-section of pin fins (Sahiti et al., 2006)

From their experiment they observed that the flow around a staggered pin fin array is characterized with one impact point where the boundary layer starts to develop in two symmetrical parts around the pins. The boundary layer separation takes place at different angles depending on the cross section. It was observed that for the circular and lancet cross sections, the angle between the stagnation point and separation point is smaller than for the drop, elliptical and NACA cross sections. For the square cross section, the boundary layer

separated immediately after the rear corner of the profile, with particularly noticeable vortices compared to the other profiles.

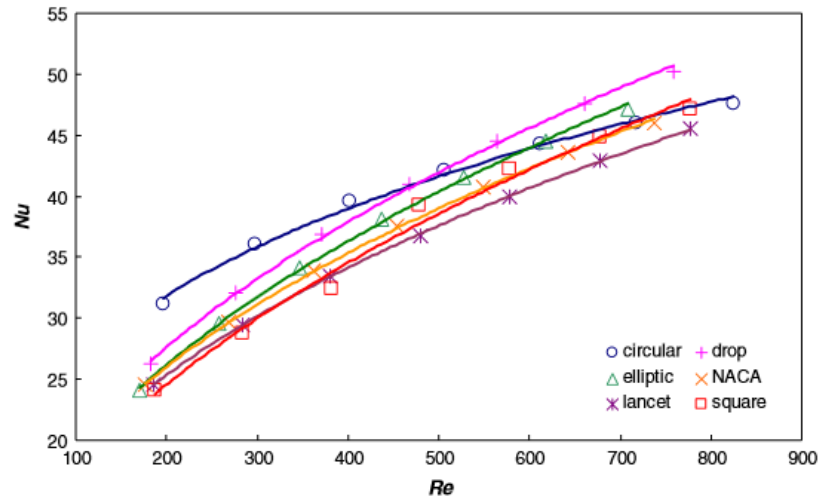


Figure 2-2: Pin fin array Nu as a function of Re (Sahiti et al., 2006)

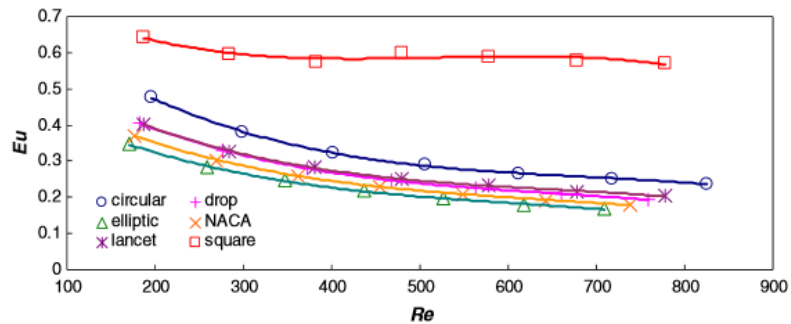


Figure 2-3: Pin fin array Eu as a function of Re (Sahiti et al., 2006)

Figure 2-2 and Figure 2-3 represent the performance of the pins with respect to heat transfer and pressure drop across the channel. It can be observed that with respect to heat transfer levels the circular pin fins show the highest levels of heat transfer. However, with respect to pressure drop across the channel the circular pins do not perform as well as most of the other cross sections, with the square cross section showing the biggest pressure drop.

As discussed earlier, pin fin channels are usually used on the trailing edge of the blades. Most of the experimental studies carried out is restricted to flow normal to pin fins where the pin fin length and duct cross sectional area are kept constant. However, the trailing edges of airfoils usually have a wedge shaped cavity as the blade tapers towards the end. Therefore, it is important to study the effects of heat transfer and pressure drop in a converging pin fin cooling channel. Hwang and Lui (2002) conducted experimental analysis to study end wall heat transfer and pressure drop in a wedge shaped duct inserted with an array of circular pin fins. They examined the effects of flow orientation, pin arrangement and Reynolds number on end wall heat transfer. Figure 2-4 represents the wedge duct used with different orientations of outlet flow.

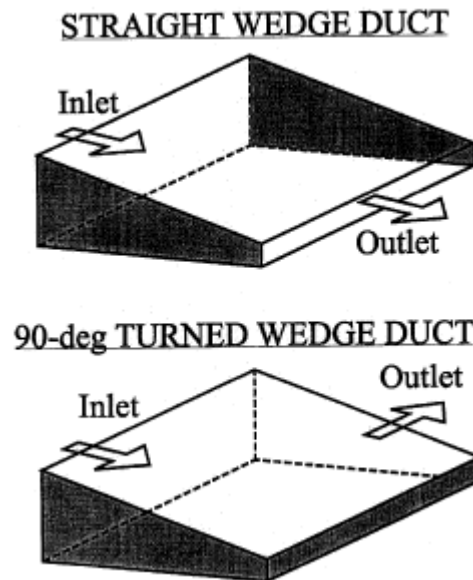


Figure 2-4: Wedge ducts of different orientation of outlet flow (Hwang & Lui, 2002)

The experimental work provided new information of detailed heat transfer distributions on the end wall surfaces of the wedge shaped duct. It was observed that heat transfer coefficient at the end walls increased with an increase in row number due to the

flow acceleration effect which is different from the trend observed from that of a duct with a constant cross sectional area. A staggered array produced about 15% higher end wall averaged heat transfer compared to an in-line pin array. It was also observed that turning the flow laterally from the straight exit reduced end wall averaged heat transfer by about 15% for the staggered array and 30% for the in-line array. Overall, a wedge duct with a staggered pin fin array was most recommended since it produced the highest end wall heat transfer with a moderate pressure drop penalty.

Peles et al., (2005) studied the effects of forced convective heat transfer across a pin fin micro heat sink. The objective of the study was to minimize the base temperature of the surface the pin rested on, while maintaining pressure drops as low as possible. Adiabatic tests were performed over a wide range of flow rates and pressure drops. Pressure drop across the channel was recorded using friction factor as a function of Reynolds number.

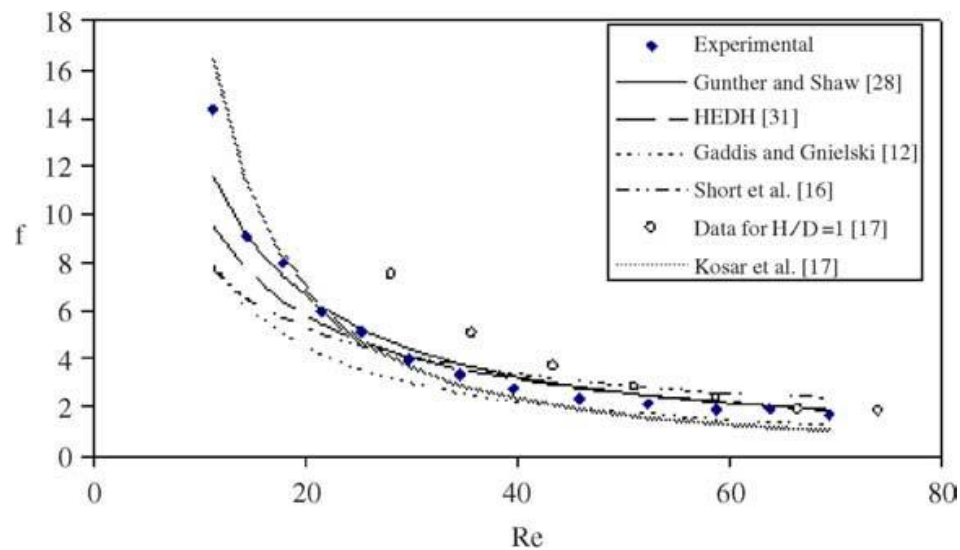


Figure 2-5: Friction factor as a function of Reynolds number (Peles et al., 2005)

Figure 2-5 is a representation of friction factor as a function of Reynolds number along with several laminar flow correlations. Peles's data correlates fairly well with the

margin of error ranging from 11.1% to 27.7%. Figure 2-5 also shows that with increasing Reynolds number, the pressure drop across the channel also increase.

Uzol and Camci (2005) experimentally studied the heat transfer, and pressure loss characteristics of staggered two-row circular and elliptical pin fin arrays. They tested two different types of elliptic pins, one was a standard elliptic fin and the other based on a NACA four digit symmetric airfoil shape. The results were compared to a corresponding circular pin fin array. It was observed that for the circular fin array, the average Nusselt numbers on the end wall within the wake was 27% higher than the standard elliptic and NACA shape pins. The pressure loss in the circular fin channel was found to be 46.5% higher than the standard elliptic fin array and 59.5% higher than the NACA shape pin array. Wake flow field measurements showed that the circular fin array created a relatively large wake zone compared to the elliptic fin arrays. The turbulent kinetic energy levels within the wake of the circular fin array was also found to be higher than that of the elliptic fin arrays. High levels of turbulence in the wake correspond to high local heat transfer rates.

Chang et al., (2008) studied the effects of attached and detached circular pin fins on heat transfer and pressure drop in a rectangular channel. The study focused on understanding the thermal performance of detached pin fins with very small pin-tip clearances from the untouched wall. The study noted that the detached pin fins offered additional convective cooling areas on the pin-tips and over the untouched wall. They obtained detailed end wall heat transfer distributions at a $C/d = 0, 1/4, 1/2, \text{ and } 3/4$ at $Re = 10,000, 15,000, 20,000, 25,000 \text{ and } 30,000$ with the pressure drop characteristics examined.

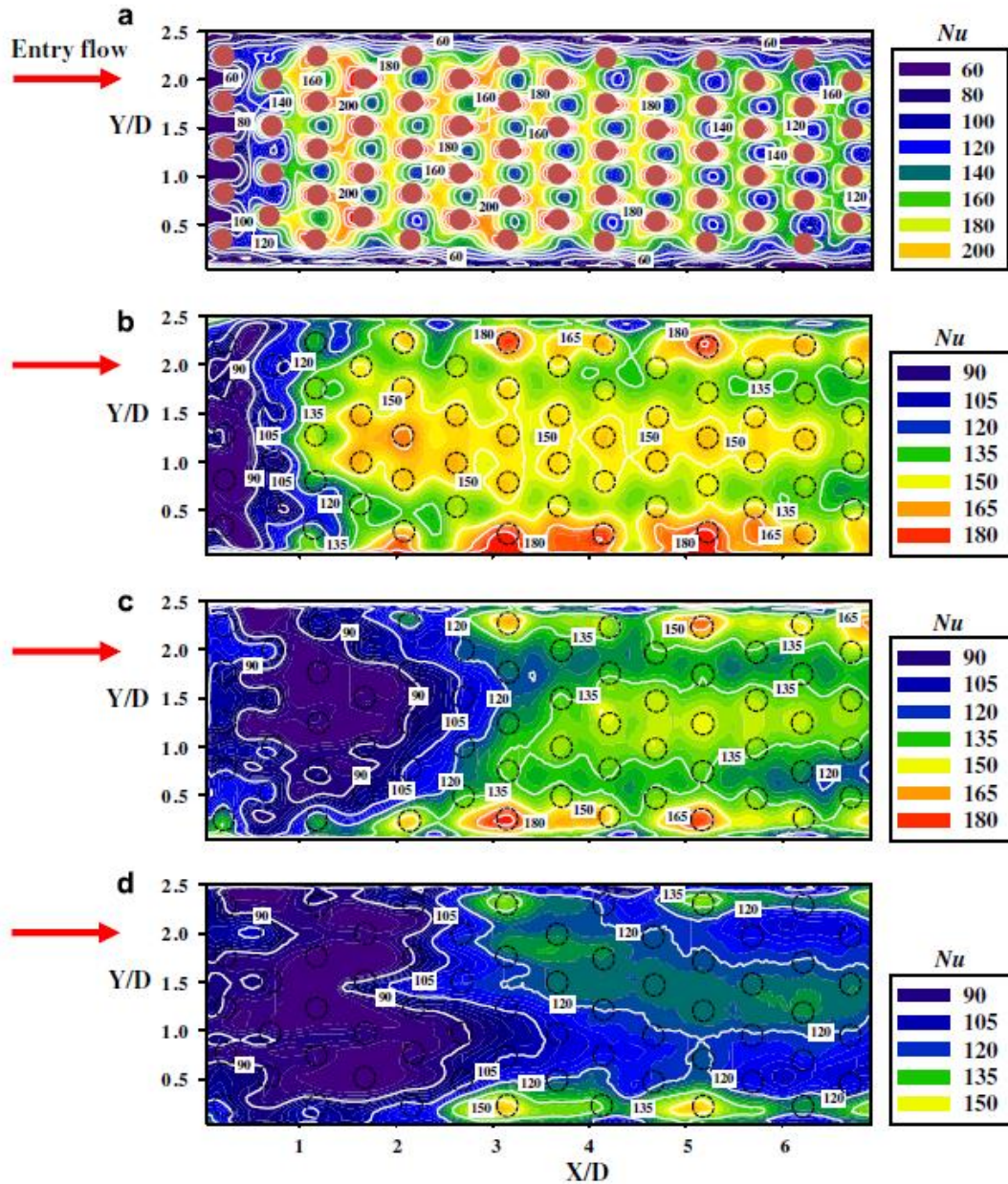


Figure 2-6: End wall Nu distributions for test channels with (a) attached pin-fins (b) detached pin-fins of $C/d = 1/4$, (c) detached pin-fins of $C/d = 2/4$ and (d) detached pin-fins of $C/d = 3/4$ at $Re = 30,000$. (Chang et al., 2008)

From Figure 2-6 it is evident that for the case with the attached pins, the effects of wake shedding and turbulent mixing of the flow result in high Nu regions at the leading edges and trailing edges of the pins. The horseshoe vortices formed upstream of each pin at the end walls also contributes to the higher heat transfer enhancement. For the attached

pins it is also observed that the levels of heat transfer increase going from the first to the third row, after which it periodically steadies out. The study observed that for the detached pin fins, although the flow mechanisms change a little, the vortex-shedding process as well as the enhanced turbulence mixing tripped by the protruding pins prevail over the mainstream. For the attached case, the end wall boundary layer was broken up by the horseshoe vortices, but for the cases with the detached pins, the accelerated flow through the gap between the pin tip and the end wall modified the boundary layer behavior. The streamwise velocity within the detached array was low and uniform, while the streamwise velocity above each pin-tip in the gap was much higher. Local heat transfer effects due to accelerated shear layers in the gaps above pin-tips are systematically faded when the C/d ratio increases from $1/4$ to $2/4$ and vanished as $C/d = 3/4$.

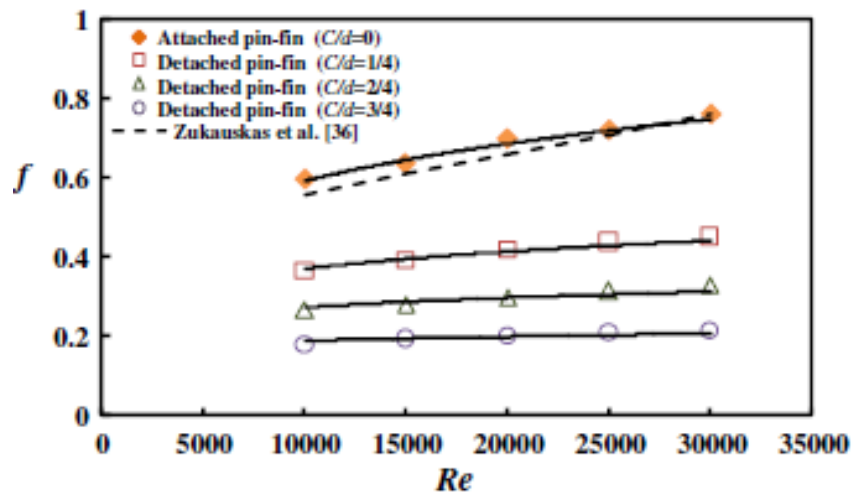


Figure 2-7: Variation of friction factor with Re (Chang et al., 2008)

Figure 2-7 represents the variations of Fanning friction factor against Reynolds number for the four test channels with $C/d = 0, 1/4, 1/2$, and $3/4$. For each of the test cases with the attached and detached pins, friction factor increases with the increase of Re. The plots in Figure 2-7 also show a significant reduction of friction factor values in the detached pin

channels from the reference condition defined by the attached pin fin channel. The f values in the detached pin-fin channels with $C/d = 1/4$, $2/4$ and $3/4$ fall considerably to the levels about 0.6, 0.43 and 0.29 times of the Fanning friction factors in the attached pin fin channel. In this respect, the absence of pin-junction mechanisms over one end wall in the channel with detached pin-fins of $C/d = 1/4$ had considerably reduced the pressure drop penalties with only minor reductions in the end wall Nu values.

2.3 Biomimicry Cooling Channel

In recent years researchers have been looking at imitating nature to help solve the issue of flow separation around a cylinder that creates areas of adverse pressure gradients.

Shyam et al., (2015) studied the effect of seal whiskers on drag reduction. Seal whiskers possess undulations along their length. He observed that the undulations on the seal whiskers have been shown to reduce vortex induced vibrations and reduce drag when compared to appropriately scaled cylinders and ellipses.

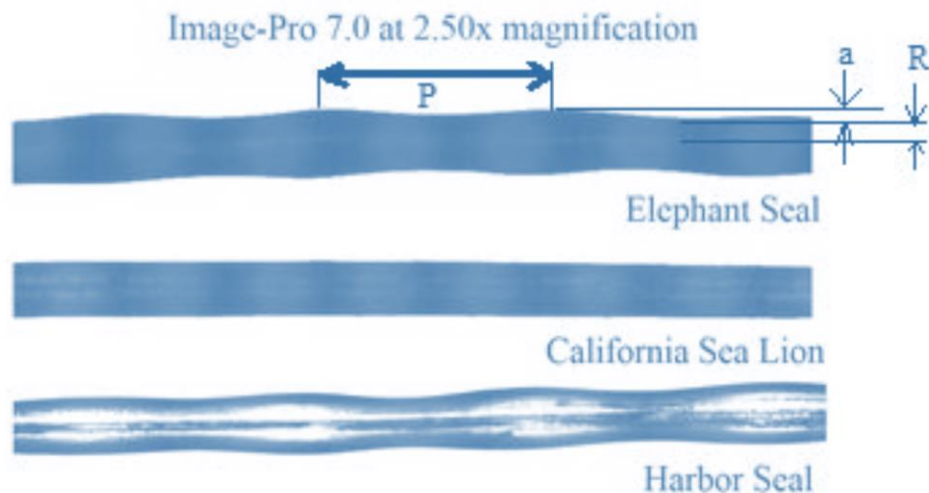


Figure 2-8: Scans of Pinniped vibrissae using optical microscope showing vibrissae parameters (Shyam et al., 2015)

The undulations observed on the seal whiskers was applied to the geometry of a blade such that the leading edge undulations match the undulations of the seal whiskers. Performance and sensitivity analyses were carried out on the various parameters involved such as pitch of undulations, angle of inclination, turbulence in the free stream and Reynolds number. It was observed that the undulations on the blade confined flow separation and regions of adverse pressure gradients to the valleys along the trailing edge of the blades. Figure 2-9 shows a comparison between a normal turbine blade and a blade designed applying the undulations observed on the seal whiskers.

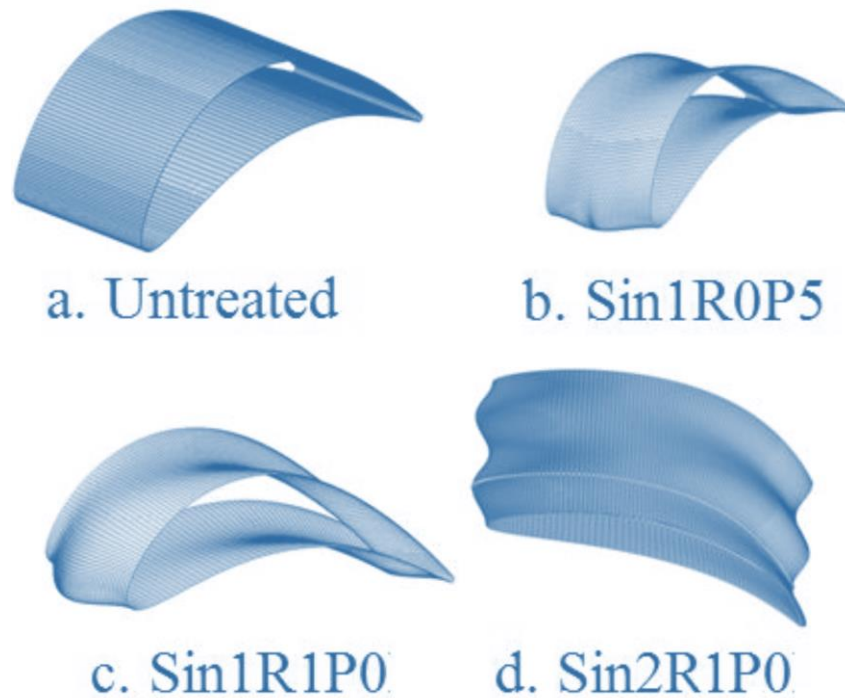


Figure 2-9: Blades geometries simulated in CFD (Shyam et al., 2015)

From the study it was observed that along the peaks, separation was almost eliminated. The averaged total pressure loss coefficient was computed to be approximately 50% lower than an untreated blade. It was also observed that the lift on the airfoil was significantly increased at the location of the peaks while not changing much at the location

of the valleys. Figure 2-10 shows a plot of total pressure loss coefficient that is an indication of drag for a wide range of incidence angles.

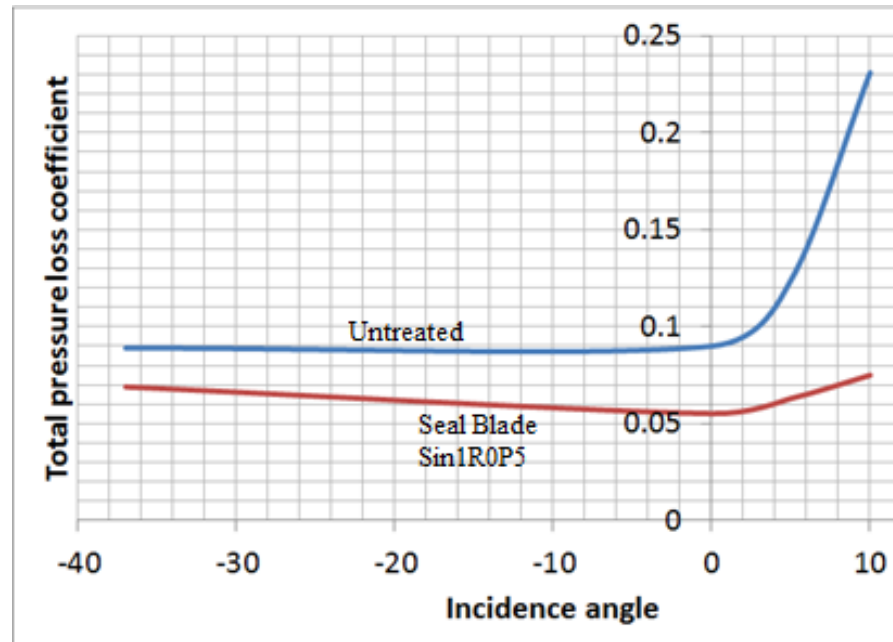


Figure 2-10: Incidence tolerance - Comparison between baseline VSPT blade and S1R0P5 over a wide range of incidence angles (-37°, 0°, 5° and 10°) (Shyam et al., 2015)

Overall the study demonstrated that the treated turbine blade could lead to almost a 50% reduction in drag. It was also observed that smaller undulation pitch has a larger benefit on performance and that the amplitude of the undulations does not have a significant effect. Also, blades with the seal whisker treatment were shown to be insensitive to incidence tolerance.

A study conducted by Hanke et al., (2010) also focused on understanding the effects of the undulations on seal whiskers. They observed that while swimming harbor seals keep their whiskers perpendicular to the swimming direction. They focused on understanding how harbor seals cope with the flow resistance on their whiskers and with vortex induced vibrations i.e. the oscillations due to vortex shedding that occur when an object is dragged

through water. They believed the solution might lie in the morphology of the whisker i.e. undulated surface structure with an elliptical cross section.

Hanke et al., (2010) conducted CFD analysis on the undulated seal whisker structure with a DNS approach in order to obtain information and visualize the effects of the unsteady flow spatial structure.

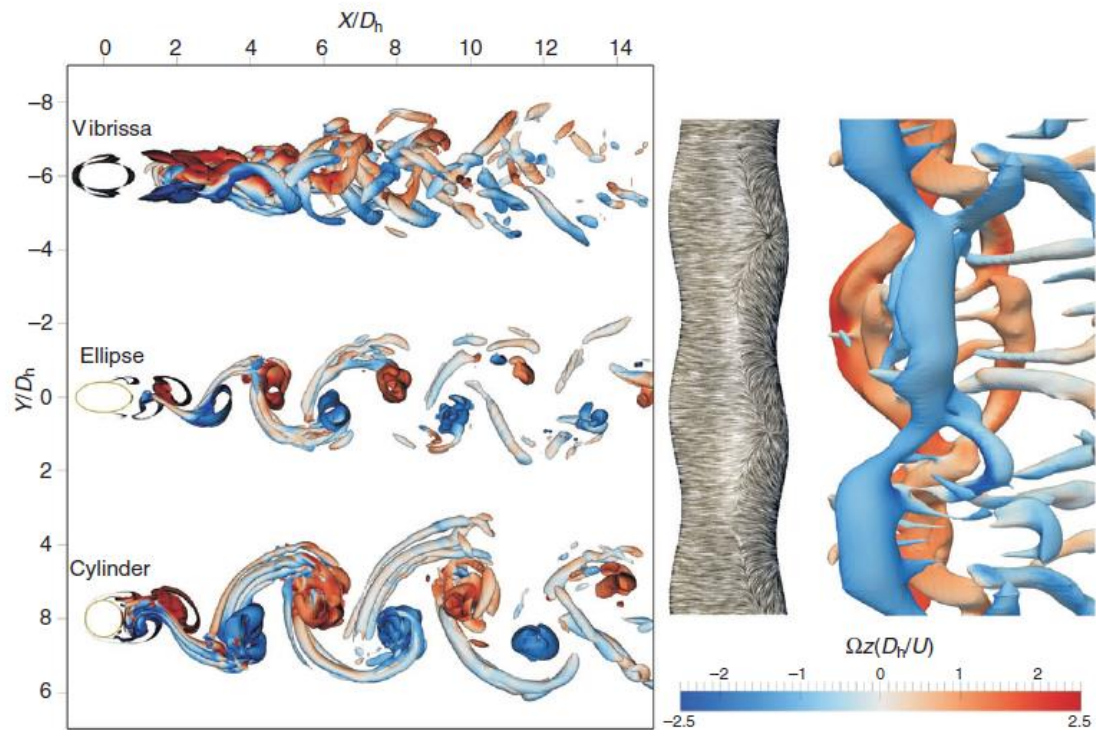


Figure 2-11: Numerical simulation of the wake-flow behind different cylinder bodies (Hanke et al., 2010)

Figure 2-11 shows the numerical solution of the wake-flow behind different cylinder bodies at a Re of 500, vortex cores depicted as isosurfaces using the Q-criterion. From the simulations it was observed that region of vortex formation is considerably shifted downstream compared with the circular or elliptic wake, showing a considerable reduction in drag.

3. Pin Fin Channel Benchmarking Study

3.1 Pin Fin Computational Set-up

To fulfill the objective of understanding the limitations and inaccuracies involved with some of the turbulence models available today, a benchmarking study was conducted that compared experimental data with computational data. The present study compared pin fin surface Nusselt numbers against the experimental case detailed by Ames et al. (2006). This experimental case was chosen due to the quality of data available, particularly the circumferential variations in Nu about the pin centerline. Computational data was also obtained as circumferential variations of the parameters of interest. Comparing the circumferential distributions helped to identify the quality of matching of the turbulence models. Figure 3-1 represents the experimental set up used for the benchmarking study.

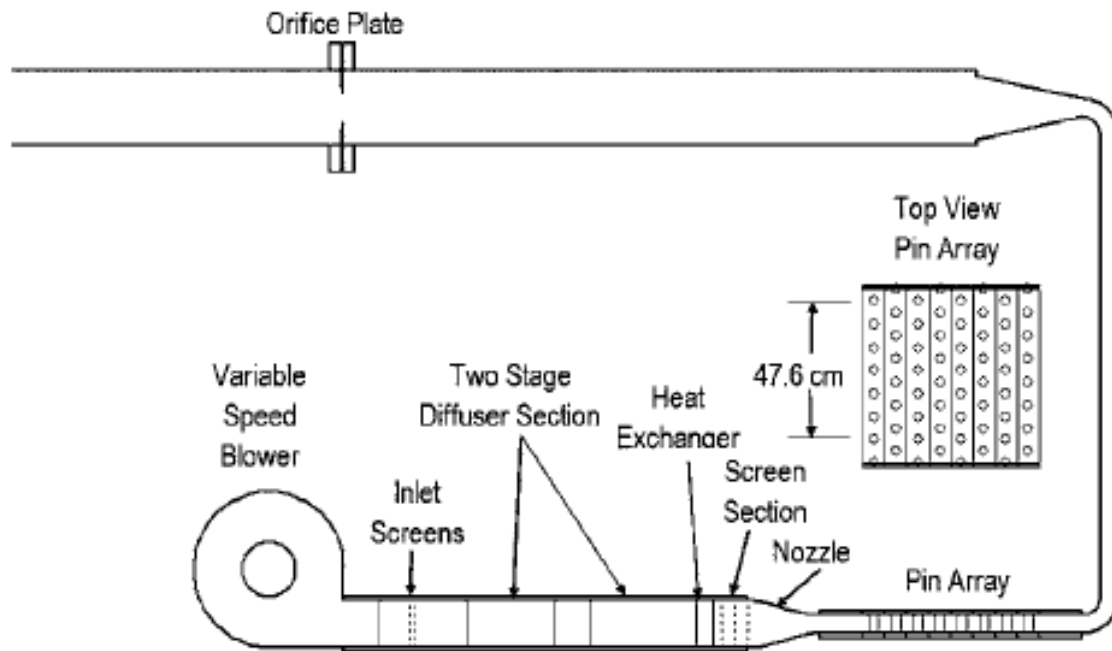


Figure 3-1: Internal heat transfer and flow facility showing staggered pin fin array test section (Ames et al., 2006)

Ames et al. (2006) studied the fluid dynamics of a staggered pin fin array using hot wire anemometry, particularly the experimental case with 8 staggered rows of 7 and a half 2.54 cm diameter pins with $S/D = 2.5$, $X/D = 2.5$, and $H/D = 2$. Data at Reynolds numbers of 3,000, 10,000 and 30,000 was available. Data was represented as circumferential variations in Nu about the midline of the pin. A detailed description of surface heat transfer measurements is given in Ames, Dvorak, and Morrow (2004). Comparing the experimental data to those obtained from the computational setup helped identify the weakness in the turbulence models used, especially as the flow transitions from a region of favorable pressure gradient at the leading edge, to the unfavorable pressure gradient at the trailing edge.

In order to maintain consistency between the computational and experimental models, the geometry was created at full scale. The domain was setup with 8 rows of 2 pins. Sensitivity studies showed that periodic interfaces on either side would accommodate for identical experimental flow conditions and allow improved computational time. The computational domain in STAR-CCM+ is represented in Figure 3-2.

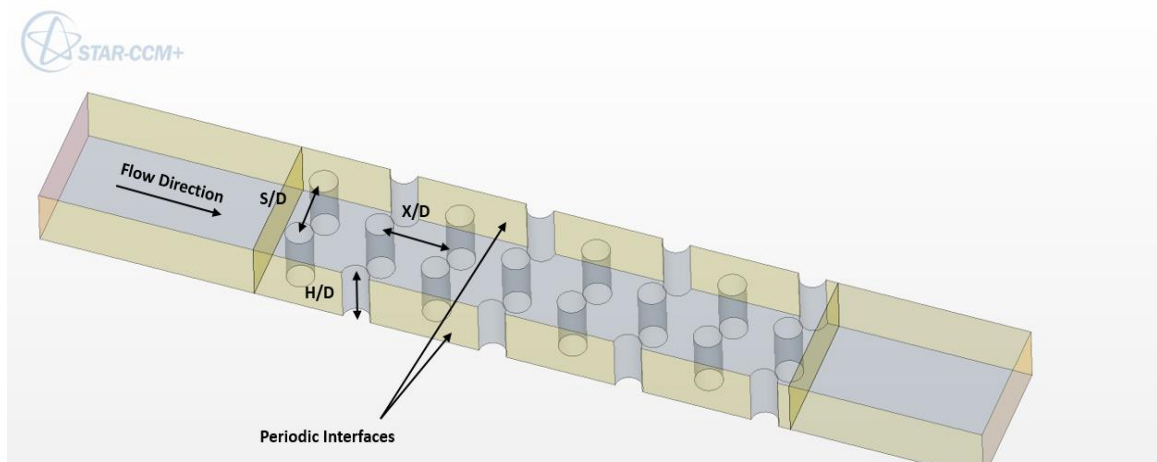


Figure 3-2: Pin fin computational domain

3.1.1 Mesh/Grid Studies

To ensure the parameters of interest were captured accurately, a mesh refinement study was carried out by changing the cell size within the computational domain. The mesh was created using polyhedral cells with a surface wrapper. The mesh/grid independence study was carried out using the quadratic form of the realizable k - ε model. A well-defined prism layer mesh was also used to capture the boundary layer effects accurately. The final mesh used for the study was determined by monitoring the mean of the average stagnation point temperature at row 1 for different mesh sizes. When the difference between temperatures at the stagnation point for 2 meshes was significantly small, the mesh with the lesser number of cells was chosen for the study, so as to save on computational cost and time. The change in the mean of the average temperature was 0.7% between the 13.9 million and 16.9 million cell cases and 0.2% between the 16.9 million and 36 million cell cases. The final mesh independent domain chosen comprised of 16.9 million cells. The 16.9 million cells case was chosen to increase computational efficiency as similar results could be obtained without the need for a finer mesh. The mesh independent study was carried out using the R-KE turbulence model. Close up images of the final mesh can be seen in Figure 3-3 and Figure 3-4. The boundary layer was fully resolved using 16 prism layers. The total prism layer thickness was set to an absolute value of 2 mm. Wall Y^+ , which is the non-dimensional wall distance for a wall bounded flow, is used to accurately capture end wall effects within the boundary layer. The boundary layer for the simulations used in the study is well resolved as the wall Y^+ is less than 1 throughout the domain.

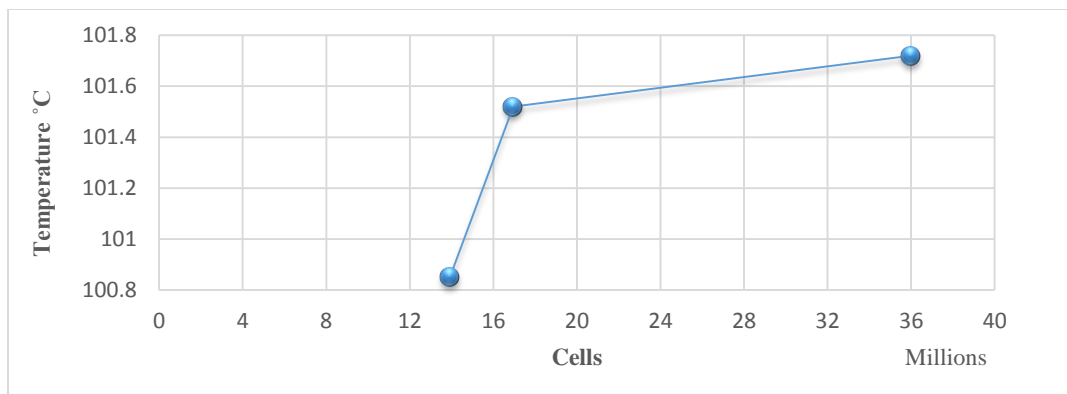


Figure 3-3: Mesh refinement study

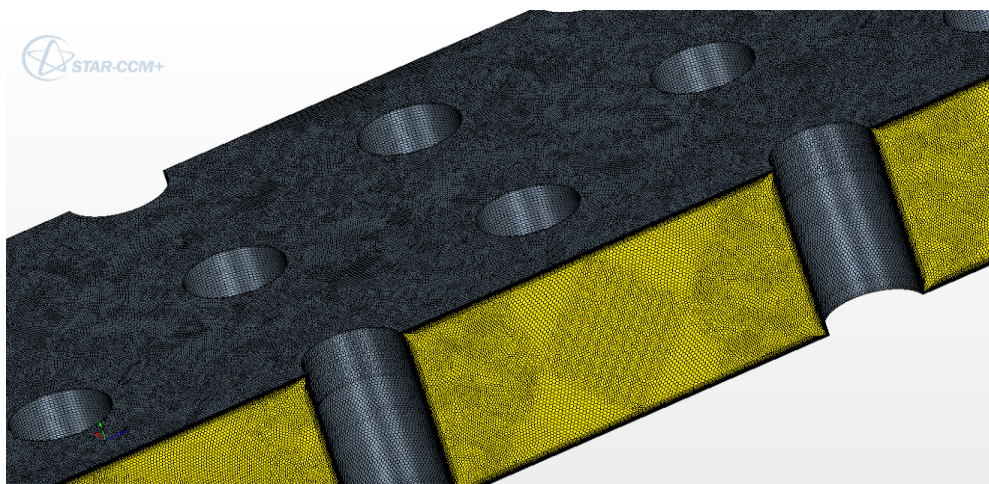


Figure 3-4: Isometric view of the final mesh

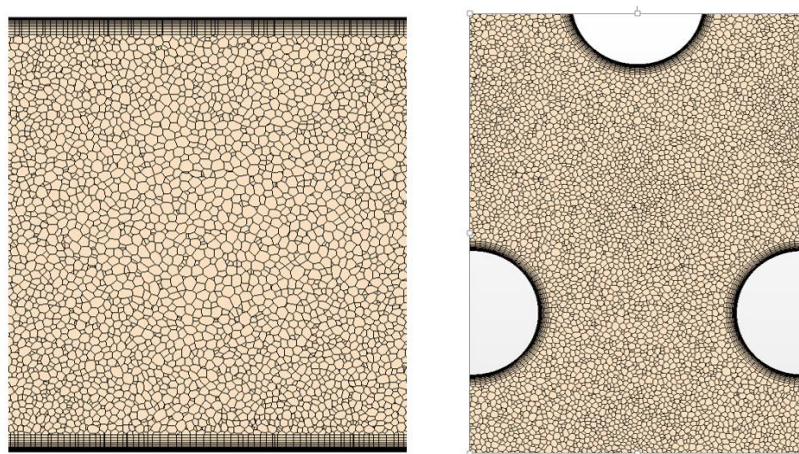


Figure 3-5: Close-up view of the mesh

3.1.2 Turbulence Models Investigated

Turbulence models in CFD have difficulty accurately predicting the flow physics at the near-wall regions. Anisotropy is dominant in the near-wall regions. These regions experience high shear stresses and high rates of turbulence, which control the skin friction and heat transfer rates. The study of the flow physics in these regions is therefore of vital importance for engineering applications. For the current study, simulations were run using the following eddy-viscosity turbulence models which are discussed briefly: Realizable k - ϵ , a quadratic form of the realizable k - ϵ model and Menter's $k\omega$ -SST. Second order models were used so as to make direct use of the governing equations for the second order moments i.e. Reynolds stresses and turbulent fluxes. The second order Reynolds stress model involved the modeling of turbulent diffusion, pressure strain correlation and turbulent dissipation rate. All simulations were run at steady state conditions.

Realizable k - ϵ model: The standard k - ϵ model solves the Navier-Stokes equations for turbulent kinetic energy (k) and turbulent dissipation rate (ϵ) from Reynolds stresses and has modifications for compressibility and buoyancy. The realizable k - ϵ model corrects the abnormal peak values of strain, hence accounts more accurately for the flow physics, as compared to the standard k - ϵ model. The non-linear Eddy viscosity models have quadratic and cubic relations for rotating flow and are expected to account for flow properties more accurately. As a consequence, the prediction of strain with respect to stress deviates largely near high normal strain regions. To account for this, the realizable option corrects the over prediction by improving the curvature formulation, keeping the strain within a range of values.

Quadratic Realizable k - ϵ model: By allowing the turbulence to have an

anisotropic effect on the flow, the quadratic non-linear constitutive relation improves the performance of the k- ϵ model, letting the model predict secondary flows better.

Menter's k ω -SST: The k- ω model on the other hand solves for kinetic energy and specific turbulent dissipation rate (ω) by blending the k- ϵ model in the free stream and adding a cross diffusion term to improve its stability. It bears a transition term (γ) to blend the two models together which effectively blends a k- ϵ model in the far-field with a k- ω model near the wall. Menter's shear stress transport model (SST) improves over the standard Wilcox model by showing more sensitivity to free stream conditions and predicting adverse pressure gradients better.

3.1.3 Data Reduction

For the pin fin benchmarking computational model, flow rates were established utilizing a velocity condition at the inlet, and a pressure outlet condition at the exit. The pin fins were provided with a constant heat flux condition of 1000 W/m². The benchmarking study simulations were run at Reynold's numbers of 3,000, 10,000 and 30,000. The Reynolds numbers were based on the effective pin approach velocity and pin diameter of 15mm. The pin diameter of 15mm was used as the characteristic length for Nusselt number calculations.

$$Re = \frac{\text{inertial forces}}{\text{viscous forces}} = \frac{\rho v D}{\mu} \quad (2)$$

3.2 Pin Fin Benchmarking Results and Analysis

Ames et al. (2006) obtained experimental pin heat transfer and surface pressure distributions about the pin midline circumference. To maintain consistency when

comparing experimental data with CFD data, the performance of the different turbulence models was analyzed in terms of Nusselt number profiles along the centerline pin surface for the mesh independent cases.

Previous work conducted within the lab by Ricklick (2014), benchmarked an experimental case conducted by Metzger et al. (1982) which showed heat transfer data for short circular cylinders in a staggered pin fin array at a Reynolds number of 53,000. Metzger (1982) observed that increased levels of turbulence and mixing downstream increased the rate of heat transfer moving from the first pin to the third pin in the array. Following the first three rows downstream, the rate of heat transfer tends to become periodically fully developed. The benchmarking study conducted by Ricklick (2014) captured this trend of increased levels of heat transfer from the first to the third row when studying the performance of a few turbulence models with a coarse and refined mesh. Figure 3-6 compares the tested turbulence models against Metzger's experimental case.

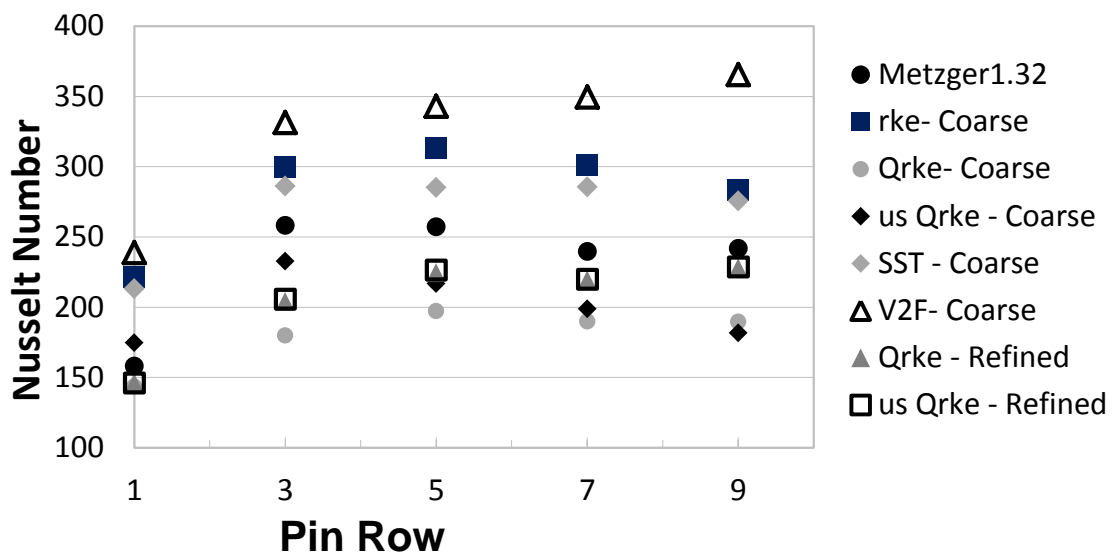


Figure 3-6: Row-by-row Pin Nusselt Number Comparison

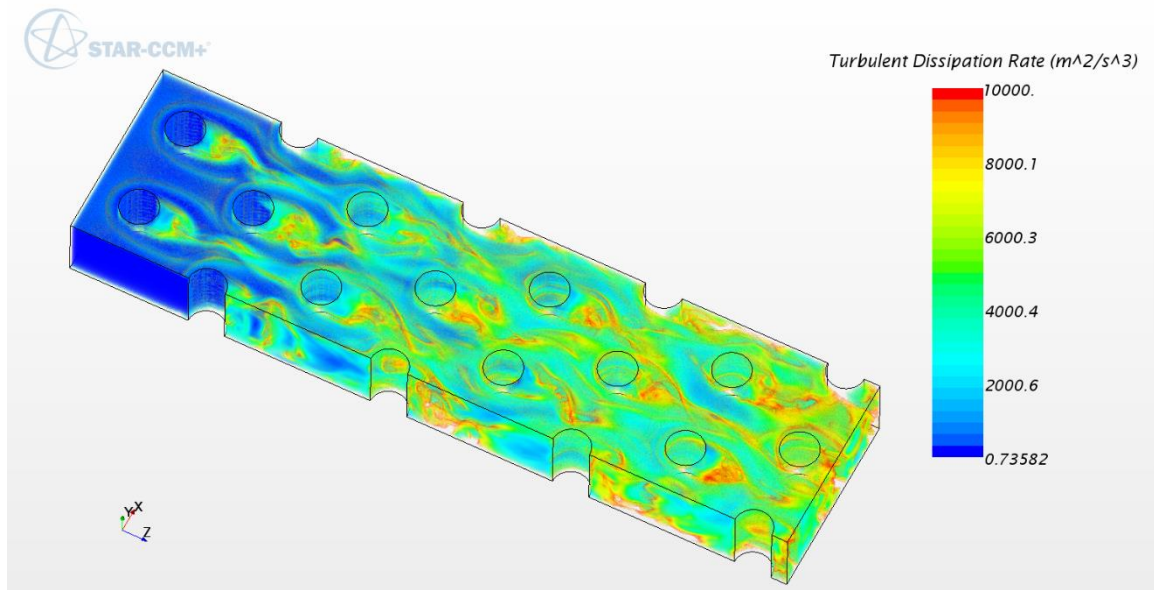


Figure 3-7: Turbulent dissipation rate $Re = 30,000$

Figure 3-7 shows that as the flow moves downstream the turbulence intensity increase. Moving from row one to row three in the array, the levels of turbulence slowly starts to increase. Past row three of the array, the levels of turbulence mixing start to steady out. The turbulent dissipation rate in the wake region of the pins increases as we move to the rows further downstream. The formation of horseshoe vortices at the end wall is also prominent in the first two rows of the array. Past the third row, the wakes from the pins upstream seem to break up the horseshoe vortex formation at the leading edge of the pins downstream.

Ames gathered data at row 1 and row 5 in the array. Comparing the CFD data to experimental data, it was observed that the levels of the turbulence models matching depended largely on the pin position in the array and on Reynolds number. Computational data will be looked at in more detail below, with data analysis and comparisons at row 1 and row 5 in the array.

3.2.1 Row 1 Heat Transfer Data

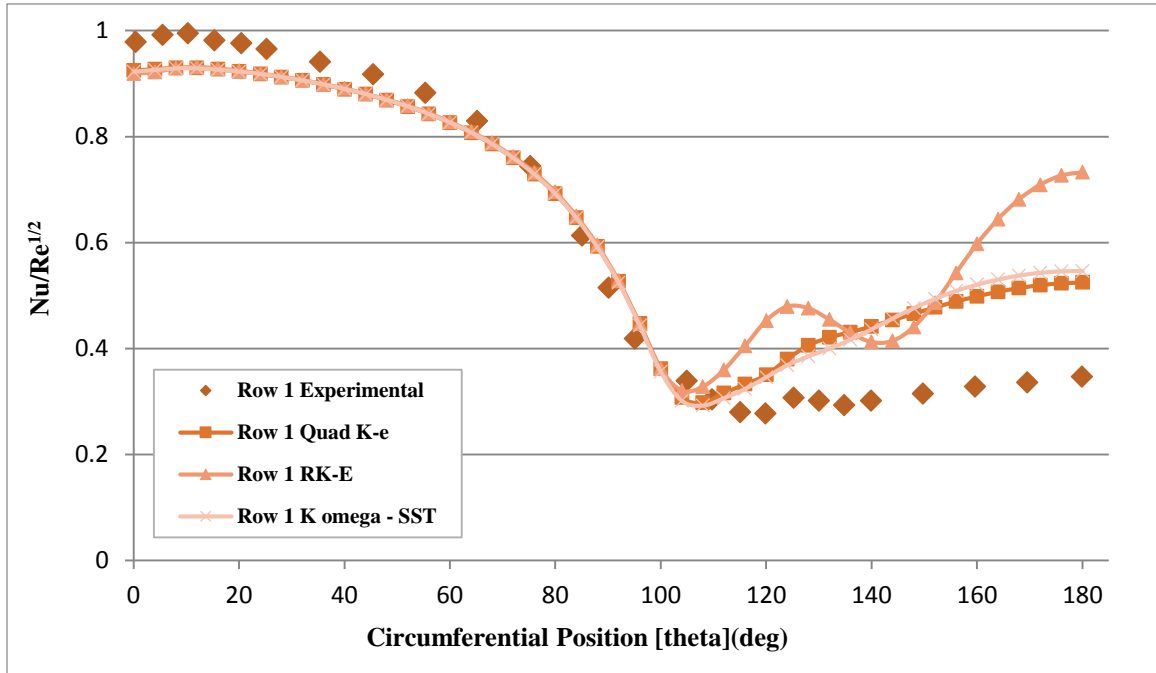


Figure 3-8: Row 1 Circumferential $Nu/Re^{1/2}$ comparison $Re = 3,000$

Figure 3-8 represents the row 1 pin midline heat transfer in terms of $Nu/Re^{1/2}$ as a function of circumferential position at a Reynolds number of 3,000. Zero degrees represents the point of stagnation on the front surface of the pin. As the flow accelerates around the pin, the adverse pressure gradients on the front and back surface of the pin cause the flow to separate which is represented by the point of minimum heat transfer. The computational models capture the general trend of the experimental data along with the flow separation point. At low Reynolds numbers, all three turbulence models closely match the trend of the experimental values. In the forward section of the pin, all three turbulence models slightly under predict heat transfer to within 6%. Experimental data shows flow separation at 120° . The QRK-E turbulence model under predicts this flow separation point by 10%, the RK-E model under predicts it by 13% and the KO-SST model under predicts it by 11%. In the trailing edge region, at $Re = 3,000$ the QRK-E and KO-SST turbulence

models over predict experimental values by about 40% whereas the RK-E models over predicts by about 60%. Overall, at low Reynolds Numbers the QRK-E and KO-SST turbulence model show a general trend that closely matches experimental data.

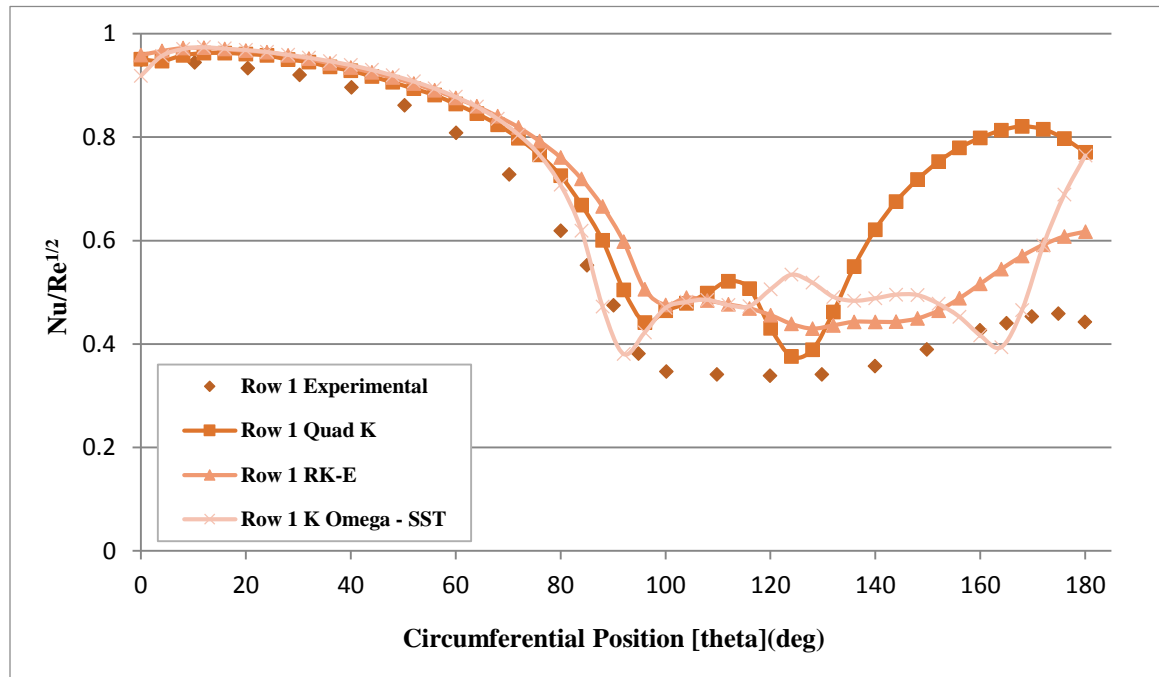


Figure 3-9: Row 1 Circumferential $Nu/Re^{1/2}$ comparison $Re = 10,000$

Figure 3-9 represents the row 1 pin midline heat transfer in terms of $Nu/Re^{1/2}$ as a function of circumferential position at a Reynolds number of 10,000. All three turbulence models match the general trend of the experimental data on the front surface of the pin, but over predict heat transfer by about 5%. The separation point of all three models is within 10% of literature data. The RK-E model predicts the point of separation closest to that of the experimental data with a slight over prediction of heat transfer at that point. Averaging the Nusselt numbers, it is observed that all 3 turbulence models over predict the heat transfer on the back surface of the pin considerably. The QRK-E models over predicts by almost 70%, whereas the RK-E and KO-SST models over predict by 25%.

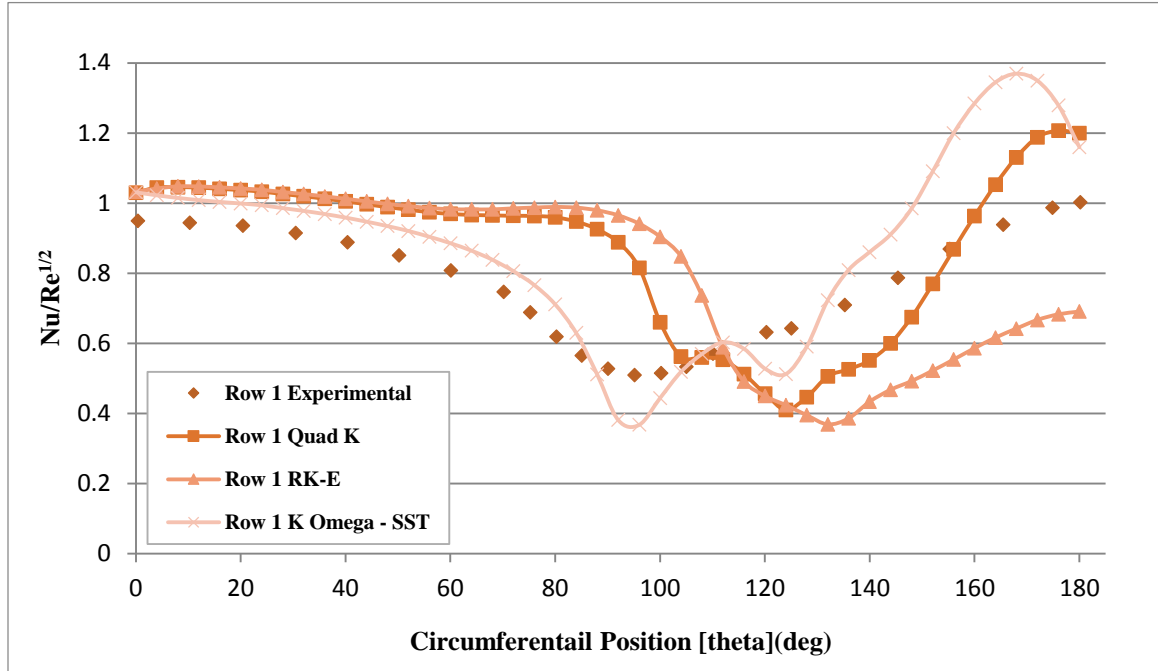


Figure 3-10: Row 1 Circumferential $Nu/Re^{1/2}$ comparison $Re = 30,000$

Figure 3-10 represents the row 1 pin midline heat transfer in terms of $Nu/Re^{1/2}$ as a function of circumferential position at a Reynolds number of 30,000. The KO-SST model maintains a 5% difference on the front surface of the pin, whereas the QRK-E and RK-E models over predict heat transfer by almost 20%. The KO-SST model also under predicts flow separation by 8%, whereas the QRK-E and RK-E models over predict the point of separation by 27%. When averaging the Nu on the back surface of the pin, the QRK-E model over predicts by 18% and the RK-E model under predicts by 30%. On the other hand, the KO-SST model matches the trend of the experimental data on the back surface closer compared to the other models, over predicting heat transfer by 12%.

The back surface of the pin is dominated by regions of turbulent wakes and adverse pressure gradients. The KO-SST model is more sensitive to free stream conditions and solves for turbulent dissipation rates by predicting adverse pressure gradients better.

Therefore, at $Re > 10,000$, the KO-SST turbulence model matches the trend of the experimental data better than the QRK-E and RK-E models. As Reynolds number increases the k-Epsilon models struggle to accurately match experimental data. It is also observed that the KO-SST model does better than the k-Epsilon models in predicting separation and re-attachment.

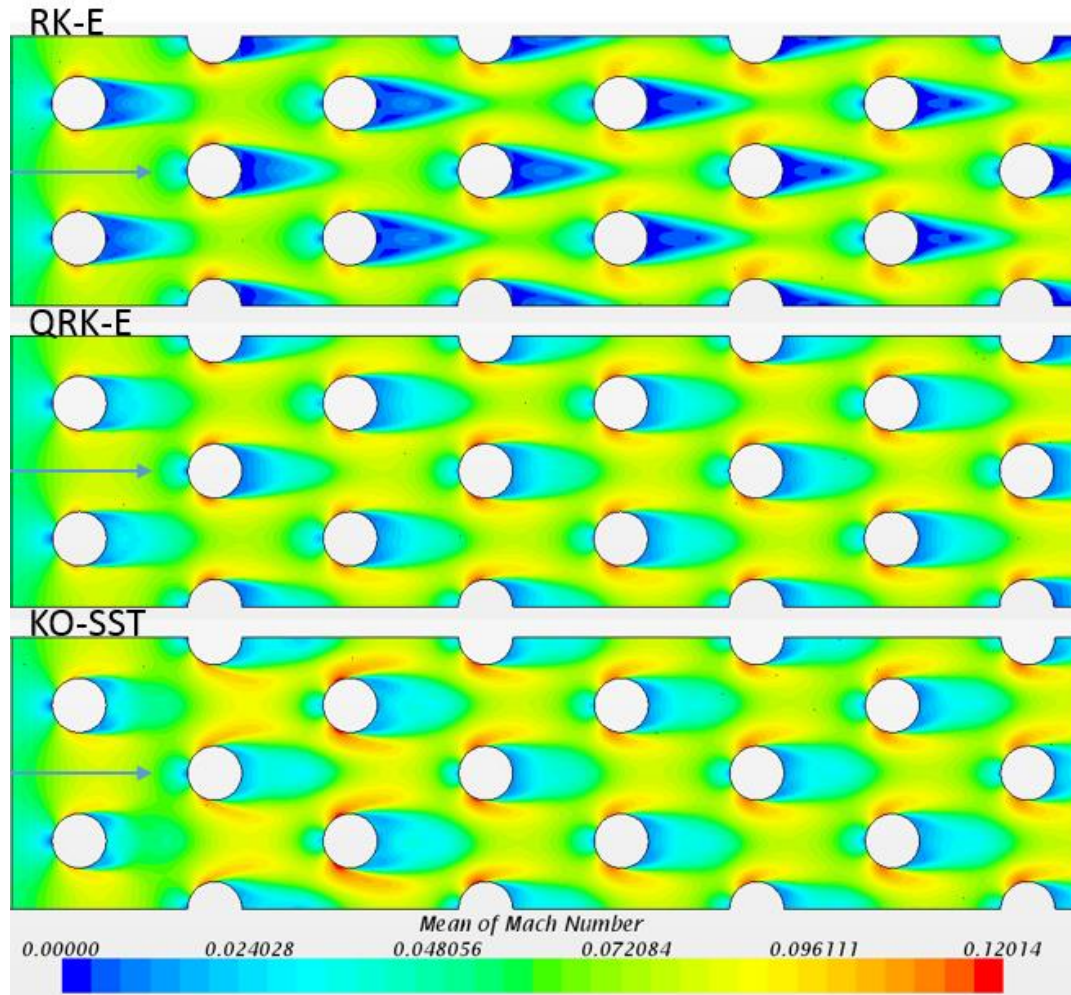


Figure 3-11: Comparison of mid-plane Mach number contours $Re = 3,000$

Figure 3-11 is a representation of the Mach number contours from the different turbulence models studied. It can be seen that the wake flow is resolved differently for each case. The RK-E model shows the least mixing in the wake region with the QRK-E model

showing considerable mixing of the wake bulk flow downstream. The KO-SST model also shows mixing of the wake bulk flow further down the channel. This is consistent with the Nusselt number profiles shown above. The QRK-E model and KO-SST model show substantially higher levels of heat transfer in the wake region compared to the RK-E model.

3.2.2 Row 5 Heat Transfer Data

As the flow moves downstream into the array past the first row, the levels of turbulence increases as the flow mixes. At row 5, the wakes due to pins in the previous rows affects the flow physics in the region surrounding the pin. The quality of the turbulence models matching the experimental data tends to change as the flow moves down the array.

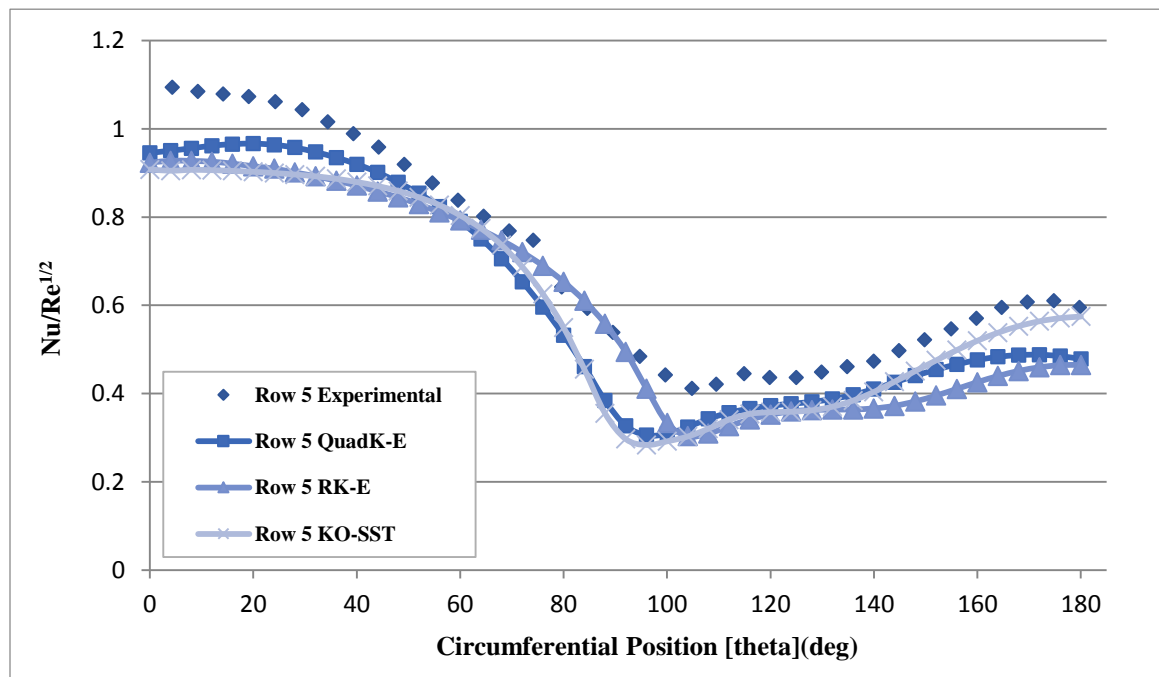


Figure 3-12: Row 5 Circumferential $Nu/Re^{1/2}$ comparison $Re = 3,000$

Figure 3-12 represents the row 5 pin midline heat transfer in terms of $Nu/Re^{1/2}$ as a function of circumferential position at a Reynolds number of 3,000. It is observed that the overall trend of the computational data matches the experimental data with the point of flow separation being within 10 degrees to that of the experimental data. CFD data also matches the trend of experimental data in the wake region behind the pin. However, although the general trend is captured well, all three turbulence models under predict the Nusselt number data by 15%. This under prediction is observed at the stagnation and wake regions of the pin. Moving down the array from row 1 to row 5, the turbulence models capture the trend of the experimental data but tend to show an under prediction in the levels of heat transfer.

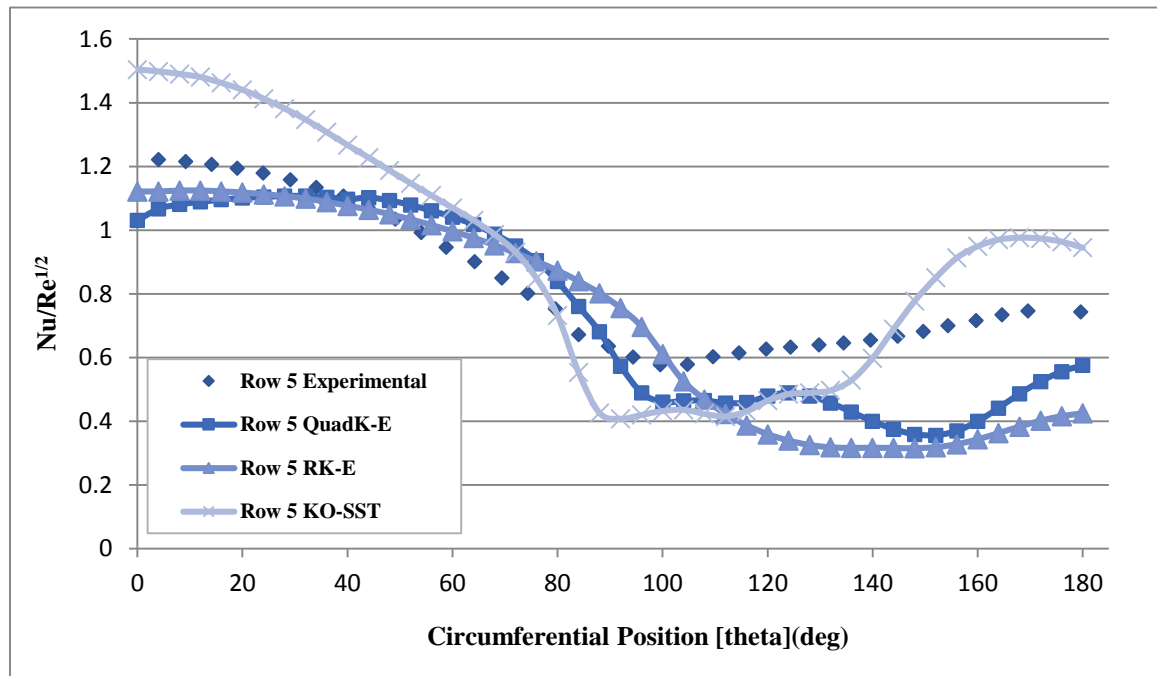


Figure 3-13: Row 5 Circumferential $Nu/Re^{1/2}$ comparison $Re = 10,000$

Figure 3-13 represents the row 5 pin midline heat transfer in terms of $Nu/Re^{1/2}$ as a function of circumferential position at a Reynolds number of 10,000. The QRK-E and RK-E turbulence models match the trend of the experimental data. Averaging the Nusselt

number data, the QRK-E and RK-E models under predict heat transfer on the front surface of the pin by 6% and on the back surface of the pin by 45%. The trend of the KO-SST model does not match the experimental data as closely as the other 2 models. However, on averaging the Nusselt numbers, it over predicts heat transfer on the front surface of the pin by 4% and on the back surface of the pin by 13%.

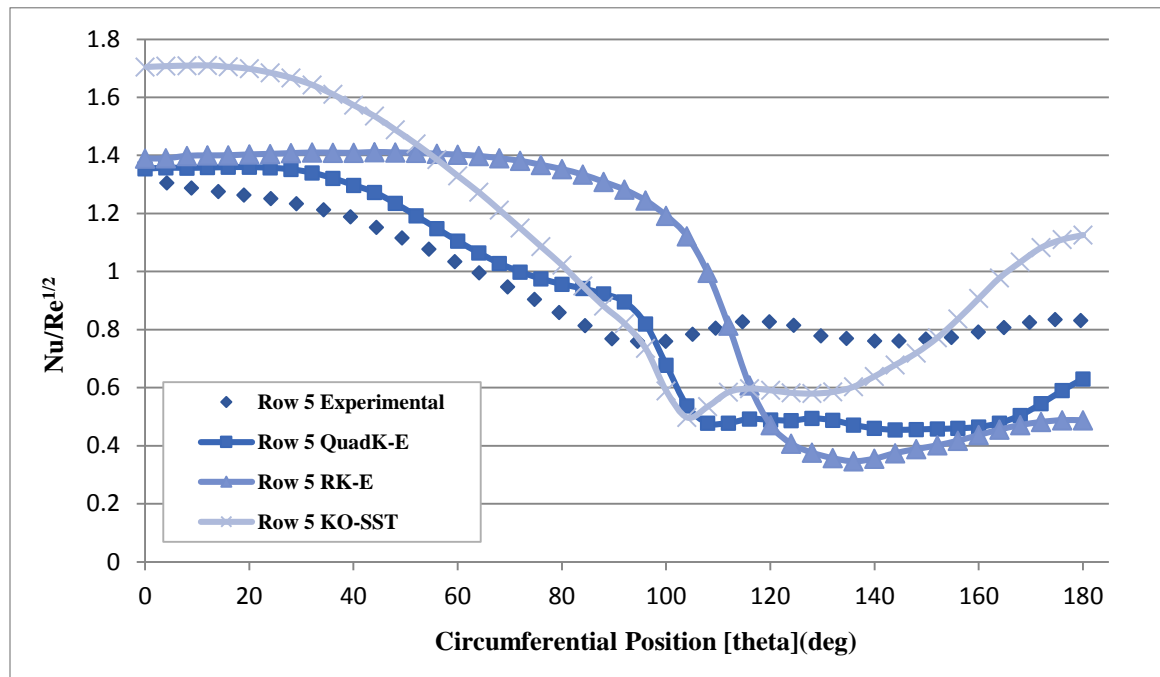


Figure 3-14: Row 5 Circumferential $Nu/Re^{1/2}$ comparison $Re = 30,000$

Figure 3-14 represents the row 5 pin midline heat transfer in terms of $Nu/Re^{1/2}$ as a function of circumferential position at a Reynolds number of 30,000. The QRK-E model matches the trend of the experimental data on the front surface with a slight over prediction of 4%. It also matches the trend of the data on the back surface but shows an under prediction of 37%. Averaging the Nusselt numbers, the KO-SST model over predicts heat transfer on the front surface by 22% with a large over prediction at the stagnation region, and under predicts heat transfer on the back surface by 5%. The KO-SST model catches the separation point closest to that of experimental data. The RK-E models doesn't fare

well at high Reynold numbers in matching the trend of the experimental data as well as capturing the point of flow separation with a substantial over prediction of the separation point.

At high Reynolds number the flow properties are more anisotropic due to an increase in the levels of turbulence in the flow channel. The RK-E model doesn't account for anisotropic flow effects and hence struggles to accurately capture the trend of experimental data at the high Reynolds number cases. The QRK-E models improves over the RK-E model by allowing the turbulence to have an anisotropic effect on the flow, allowing it to predict secondary flows better. The QRK-E models comes the closest to capturing the trend and levels of experimental data at low and high Reynolds numbers. The KO-SST model struggles to match the trend of experimental data at high Reynolds numbers but the over and under prediction tends to cancel each other out when considering the average Nusselt numbers. Although the KO-SST model does a good job of capturing flow physics at the first row of the array, it shows poor predictions as the flow moves downstream i.e. at row 5 in the array. As the flow moves downstream the turbulence intensity increases. The wake from the previous pins and the increased levels of turbulence downstream seem to affect the performance of the KO-SST model down the array for the high Reynolds numbers cases, with a substantial over prediction at the stagnation region of the pin. Overall, the higher degree of complexity in the flow downstream is captured well by the QRK-E model with closely matching trends in the front region and wake region of the pin.

3.2.3 Row 5 Pressure Data

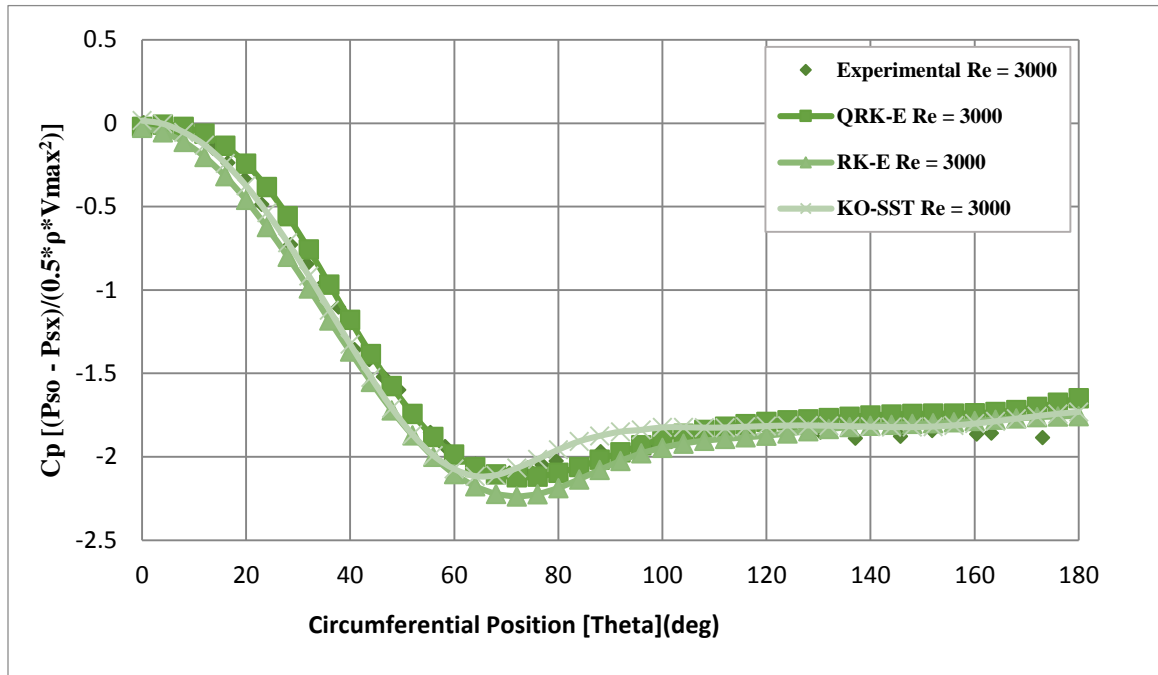


Figure 3-15: Circumferential Cp comparison Re = 3,000

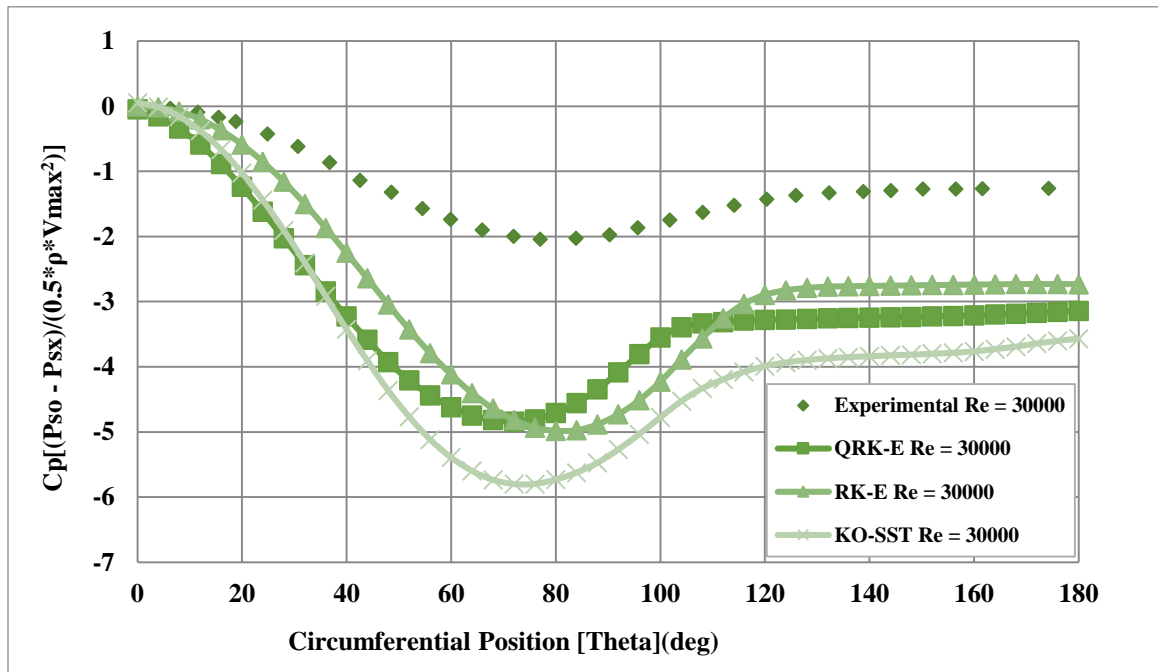


Figure 3-16: Circumferential Cp comparison Re = 30,000

Computational simulations have shown that the pressure drop across the channel increases with the increase in Reynolds number. Ames also obtained experimental data showing midline pressure coefficients along the pin at row 5. Figure 3-15 and Figure 3-16, shows pressure coefficient distributions as a function of surface angle.

Comparing the data obtained from simulations against experimental data, it was observed that at low Reynolds numbers the trend of the data of all three turbulence models matches the trend of the experimental data. At low Reynolds numbers, all three turbulence models also predict the location of the minimum value i.e. the point of separation to within 5 degrees. All three turbulence models also match the experimental pressure data to within 8%.

As Reynolds number increases, the turbulence levels in the flow increase. At very high Reynolds numbers, all three turbulence models over predict pressure coefficients after the stagnation point. Two-equation models predict an unexpectedly large growth of turbulent kinetic energy in stagnation point flows at high Reynolds numbers (Ames et al., 2004, January). This build-up of turbulence at the wake region of the pins at high Reynolds numbers is possibly the reason the turbulence models show irregularities in pressure coefficients at the back surface of the pin. The location of the minimum value from all three turbulence models is within 10 degrees. At very high Reynolds numbers, after the $\theta = 10^\circ$ point, all three turbulence models under predict the pressure coefficient. The QRK-E under predicts by 45%, whereas the RK-E and KO-SST under predict by almost 95%. After the $\theta = 110^\circ$ point all three turbulence models show substantial pressure recovery, which is the trend observed in the experimental data, however, the QRK-E model under predicts the pressure coefficient substantially. At high Reynolds numbers the pressure

recovery is substantial when compared to lower Reynolds numbers (Ames et al., 2006, January). This trend of higher pressure recovery at higher Reynolds numbers is also observed in all the turbulence models.

4. Biomimicry Channel: Seal Whisker Pin

4.1 Biomimicry Channel Computational Set-up

The computational set up of the biomimicry model was based on an original whisker geometry obtained from Shyam et al., (2015). This original undulated structure imitating a seal whisker was scaled to the size of the cylindrical pin fins studied previously which is used for internal cooling channel applications. The original geometry was scaled down and studied with two different cross-section types, one elliptical and the other of a cylindrical cross section. Previous studies have shown that the elliptical cross section showed maximum improvements in drag reduction which leads to reduced pressure losses. However, for the purposes of our study, even though reduced pressure losses in the goal, maximum heat transfer is also the major objective of the cooling channel. Conducting the study with two different cross sections allowed for feasibility studies on fluid flow characteristics as well as on thermal properties. Figure 4-1 shows the different undulated structure geometries used for the study.

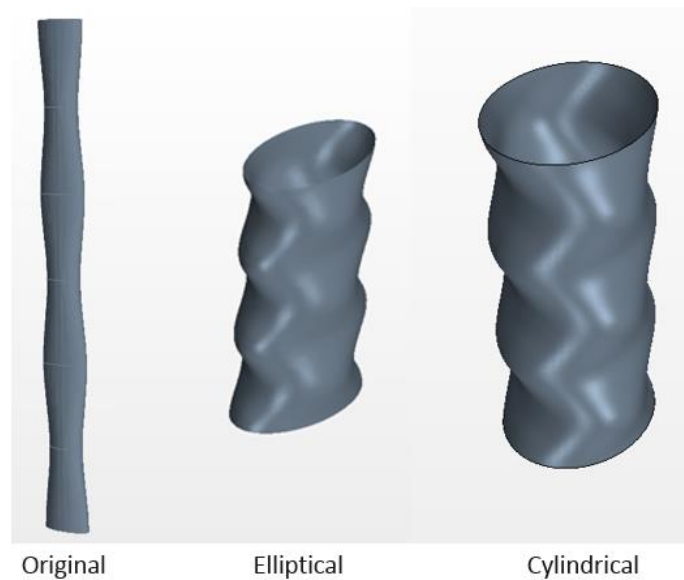


Figure 4-1: Bio Pin geometries used for the study

The computational domains for the 2 different cross sectional geometries were created using the same procedure used for the pin fin channel benchmarking case. For comparison, parameters of interest were recorded for 3 different cases, one with a cylindrical pin fin, the other of an elliptical bio pin and the third a cylindrical bio pin. The height of the pin for all 3 cases is 30 mm. The diameter of the cylindrical pin fin is 15mm. The elliptical bio pin has a major diameter of 15mm and minor diameter of 9mm. The cylindrical bio pin has a diameter of 15mm. The geometry of the internal cooling channel comprised of a staggered array of pins with a spacing of $X/D = S/D = 3$ and $H/D = 2$. Figure 4-2 is a representation of the elliptical bio pin computational domain. An identical domain was created for the cylindrical pin fin and bio pin.

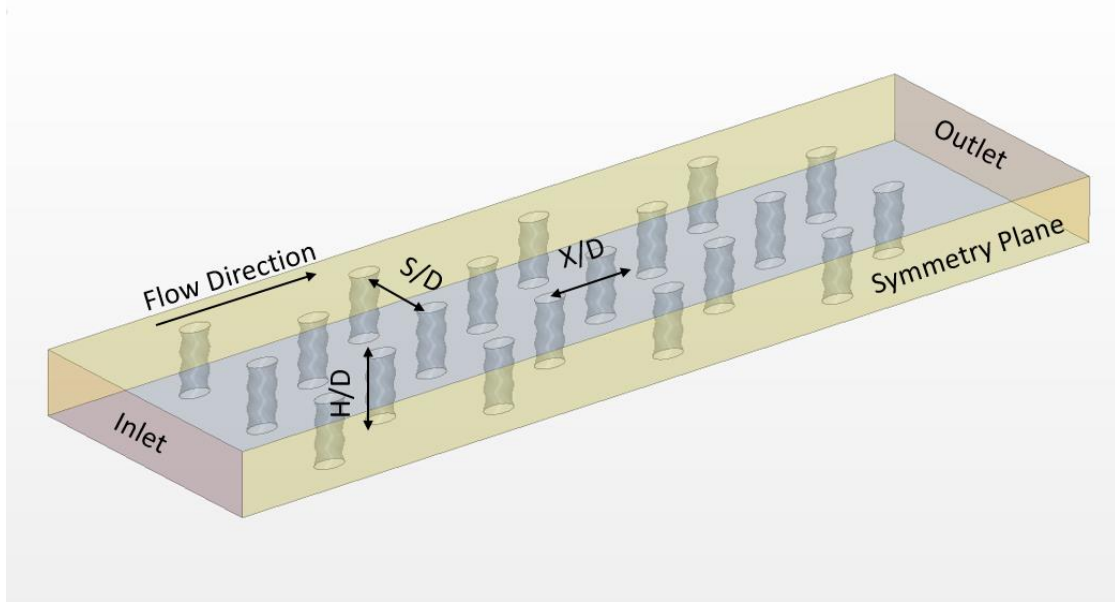


Figure 4-2: Elliptical bio pin computational domain

A mesh independent study was carried out using the average of the centerline stagnation point temperature as a reference point. The simulations were run using the quadratic formulation of the realizable k- ϵ model. The final mesh independent domain was comprised of 11.3 million cells. The boundary layer of the domain was well defined with

the boundary layer mesh of 1.75mm comprised of 10 prism layers. The Wall Y^+ is less than 1 throughout the domain, which relates to the boundary layer being well defined.

Figure 4-3 represents the mesh details of the elliptic bio pin channel.

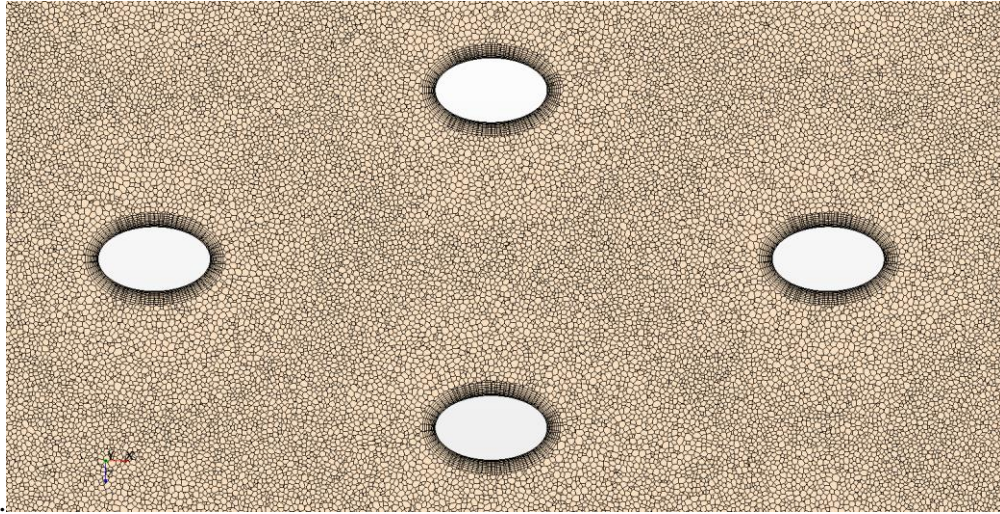


Figure 4-3: Polyhedral mesh with well-defined boundary layer

For the biomimicry (seal whisker) channel computational model, flow rates were established similarly to that of the benchmarking study case. The bottom wall and the fins were supplied with a heat flux condition of 1000 W/m^2 . The simulations we run at a Reynolds number of 5,000 which was based of the pin diameter of 15mm used as the characteristic length. The majot diameter of 15mm was used as the characteristic length for Nusselt number calculations.

4.2 Biomimicry Channel Results and Analysis

For the secondary objective of aiming to reduce the pressure drop across a pin fin channel, a seal whisker inspired geometry was employed on to the pin fin. A preliminary investigation of the flow physics and heat transfer properties of the bio pin is discussed here. Previous studies have shown that the undulations on the surface of seal whiskers help

to reduce drag. Reduction of drag leads to a reduction of pressure losses. The undulations on the whisker surface are defined by alternating peaks and valleys. Figure 4-4 is a representation of the front and side view of the pin also defining the location of the peak and valley i.e. areas of interest for the current study.

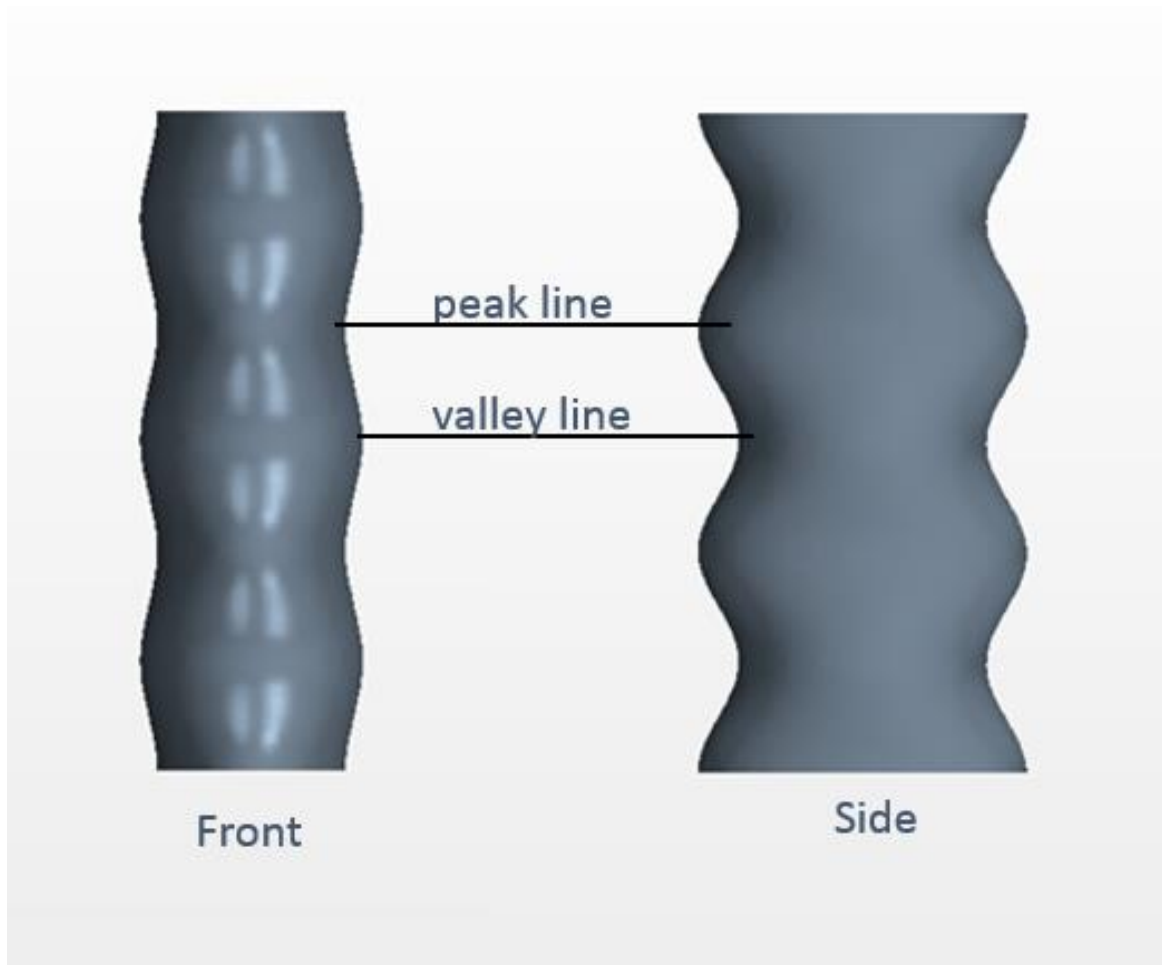


Figure 4-4: Elliptic bio pin front and side view

For the cylindrical pin fin data was acquired at the pin midline about the circumference. For the bio pins data was acquired circumferentially at the two locations defined by the peak and valley line as shown in Figure 4-4. Heat transfer data was recorded in terms of Nusselt number as a function of circumferential position.

4.2.1 Biomimicry Channel Heat Transfer Data

Figure 4-5 is a representation of the heat transfer data at row 1 of the array, as a function of circumferential position for the cylindrical pin fin, elliptical bio pin and cylindrical bio pin.

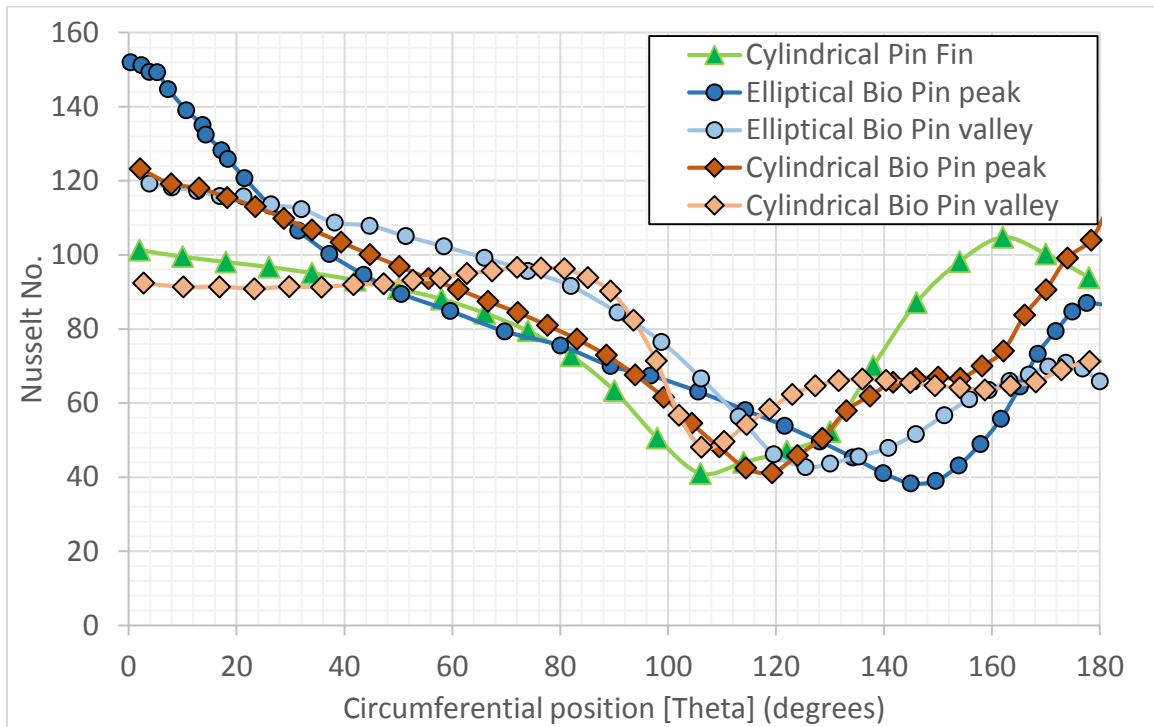


Figure 4-5: Circumferential Nu comparison Re = 5,000

From Figure 4-5 it is evident that on the front surface, the bio fins show higher levels of heat transfer compared to the cylindrical pin fin. In the region behind the pin i.e. the wake region, the cylindrical pin fin shows a higher level of heat transfer from the pin surface. For the cylindrical pin fin, flow separation occurs the earliest at 105° , which is defined by the point of minimum heat transfer. For the cylindrical bio pin the separation point at the peak and valley lines are slightly further down the pin, but close to that of the cylindrical pin fin. The elliptical bio pin show highest levels of heat transfer at the stagnation regions, and flow separation occurs the latest when compared to the other pins.

Flow separation for the elliptical bio pin occurs at 125° at the valley line and at 150° at the peak line. The wakes created on the back surface of the pins are due to the flow separating as it accelerates around the surface of the pin. The wakes are comprised of regions of high turbulence and flow vortices that act as drivers of heat transfer. Figure 4-5 shows lowest levels of heat transfer on the back surface of the elliptical bio pin. Later flow separation for the elliptical bio pin leads to smaller wakes in this region which results in lower levels of heat transfer on the back surface. Averaging the data around the circumference of the pins, the bio pins showed a 2.6% increase in levels of heat transfer over the cylindrical pin fins.

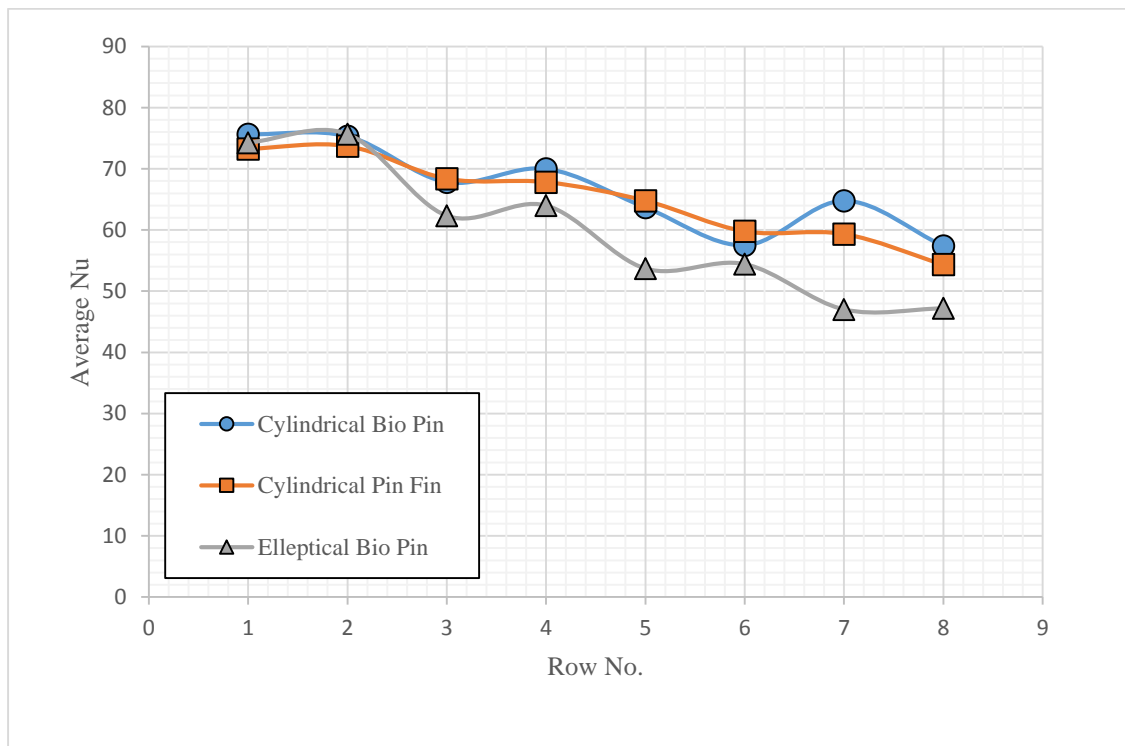


Figure 4-6: Row-by-row Pin Nusselt Number Comparison

Figure 4-6 represents the averaged heat transfer at each row for the different cases. At rows 1 and 2 the bio pins show an overall higher level of heat transfer when compared to the cylindrical pin fin. However, as we move down the array it is observed that although the cylindrical bio pin maintains a level of heat transfer close to that of the cylindrical pin

fin, the elliptical bio pin shows reduced levels of heat transfer after row 3 in the array. Overall, when averaging the levels of heat transfer across the array, the cylindrical bio pins show a 2% improvement in heat transfer when compared to the cylindrical pin fins.

4.2.2 Biomimicry Channel Pressure Data

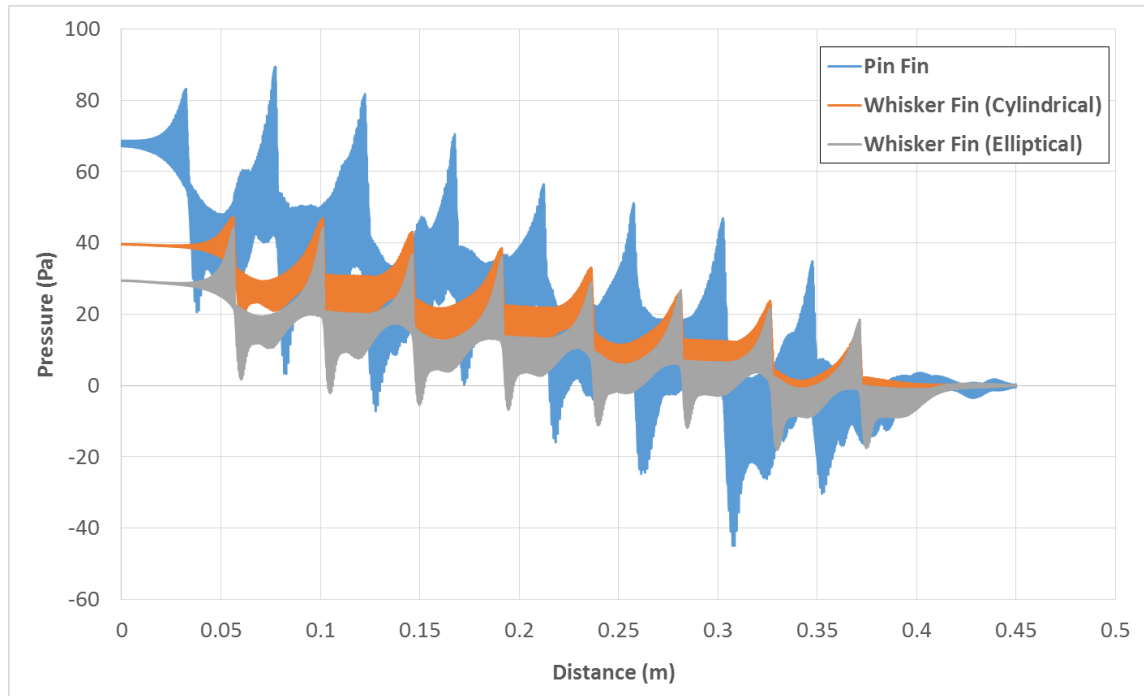


Figure 4-7: Pressure profile across the channel

Work from previous literature has shown that the undulations on the surface of seal whiskers reduces drag and thereby reduces the induced pressure losses. Figure 4-7 represents the drop in pressure across the channel. From the plot it is clearly evident that the bio pins show a smaller pressure drop across the channel over the standard cylindrical pin fin. The elliptical bio showed a 55% improvement in pressure drop loss across the channel and the cylindrical bio pin showed an improvement of 42%. The plot also shows that the pressure gradients in the wake and stagnation regions of the pin are smaller compared to that of the cylindrical pin fin.

5. Pin Fin Channel Experiment

5.1 Experimental Set-up

The last few decades has seen extensive experimental work studying the flow behavior and characteristics in a pin fin channel. Various experimental studies have been carried out to study the effect of the pin fin channel flow features on end wall heat transfer. Experimental work has also been conducted to study the heat transfer from the pin surface and flow features surrounding the pin. However, very little has been done to study the effects of both together. The experimental work carried out in this investigation aims to study the effects of end wall heat transfer due to the flow characteristics of the pin fin channel as well as due to the extraction of heat from the pin fins.

5.1.1 Experimental Rig Design

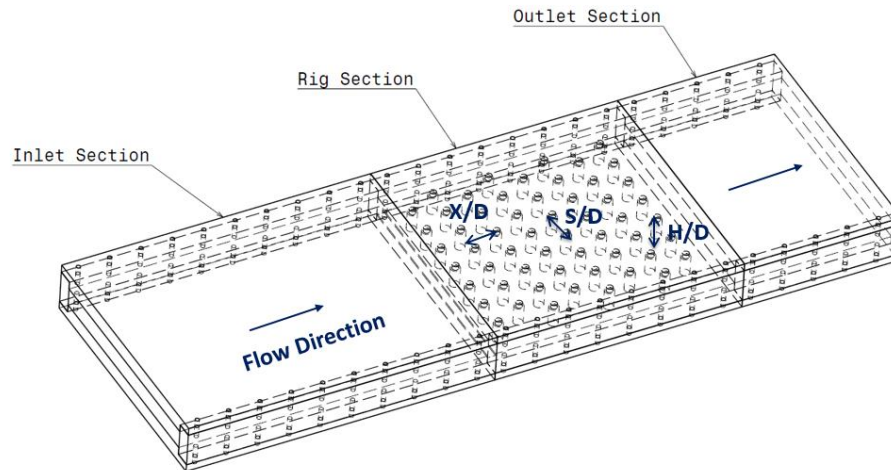


Figure 5-1: Rig Geometry

The test section was built with 1 inch thick acrylic walls and aluminum pin fins. The array comprised of 8 rows each with 7 cylindrical pins of 15 mm diameter. An array spacing of $X/D = S/D = 3$ and $H/D = 2$ was chosen for the study. As seen in Figure 5-1 an

inlet section was attached upstream of the test section to allow for the flow to fully develop before entering the test section. An outlet section was also attached downstream of the test section.

The test section was attached to a centrifugal blower downstream of the outlet section using PVC pipes. The suction side of the blower was used to suck in atmospheric air from the open end of the inlet section. A flow control valve and a venture flow meter were also attached to the piping downstream of the rig to control the mass flow rate through the test section and to be able to control the Reynolds number. Auxiliary valves were used to ensure the blower was supplied with enough air so as to prevent it from overheating. Figure 5-2 shows the experimental set up used for the study.

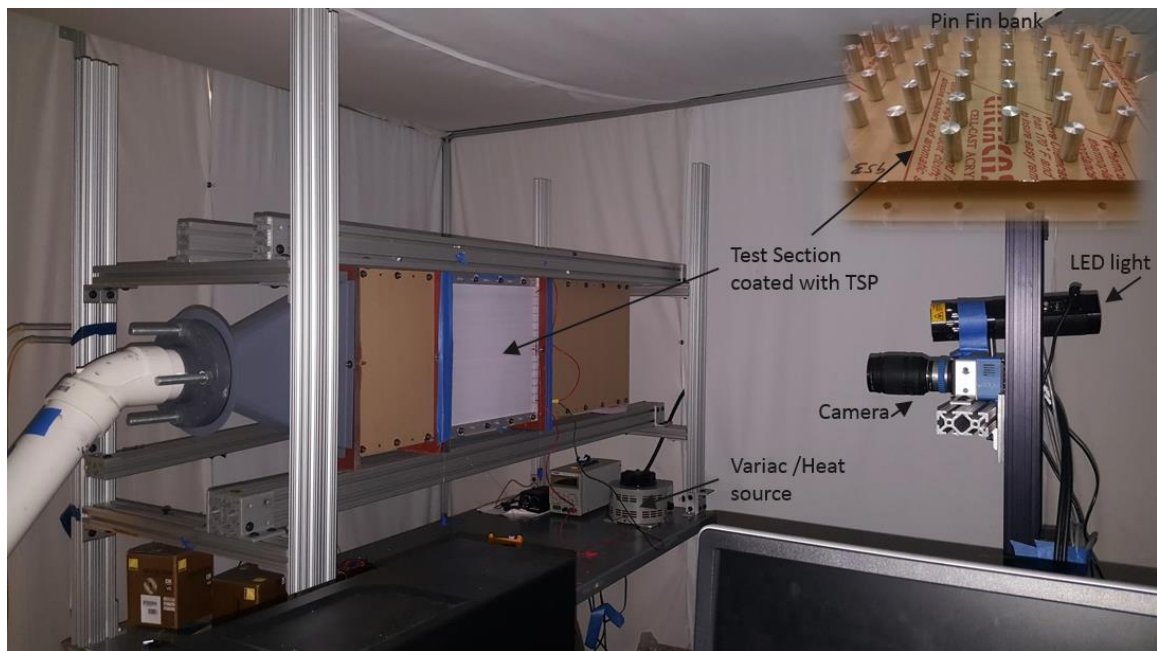


Figure 5-2: Experimental Rig Set-up

To simulate operating conditions, the bottom surface of the test section was heated using Inconel strips each 15mm in width. The Inconel strips were arranged in a snake like pattern in series which results in high resistance when a current is passed through it. Passing

an electric current through the strips generates electrical resistance which produces heat, which in turn simulates heated blade surface conditions. An electric current was supplied using a VariAC. The aluminum pins resting over the Inconel strips act as fins conducting heat from bottom surface.

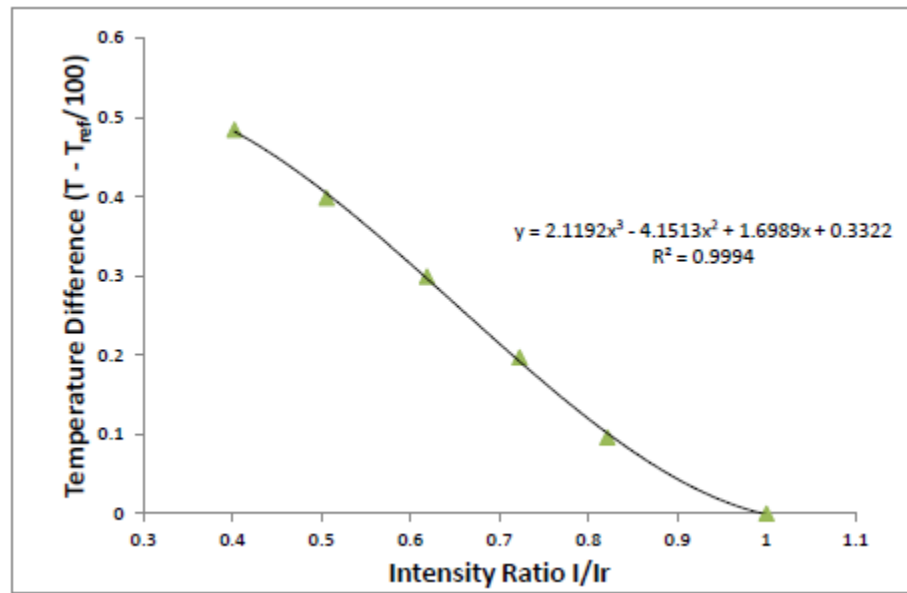


Figure 5-3: TSP calibration curve

To visualize temperature contours, the bottom surface was painted with Temperature Sensitive Paint (TSP). Temperature sensitive paint works on the principle of change of intensity with change in temperature. The paint was first calibrated to obtain a temperature-intensity curve. Figure 5-3 is a representation of the calibration curve obtained for the paint used for the experimental study. ISSI Unicoat UNT-12 TSP was the paint used for the experiment. It is comprised of luminescent paint mixed with fluorescent molecules and a binder. When activated at a particular wavelength, the paint becomes sensitive to temperature changes. Images of the TSP coated surface are captured using a scientific grade camera. The camera first captures the intensity of a reference image at a known temperature. This is followed by capturing intensities during testing condition at unknown

temperatures. Calibration curves are constructed in the form of intensity ratio vs temperature ratio. Using the captured images and the calibration curve, temperature contours can be obtained using simple post processing techniques in MATLAB. This technique of measuring temperatures was a better alternative to using a large number of thermocouples.

5.1.2 Data Reduction

The experimental rig was set-up such that the Inconel strips of 15mm width and 0.01mm thickness were attached to the bottom wall over which the aluminum pins rested. Passing an electric current through the strips of high resistance generated a heat flux.

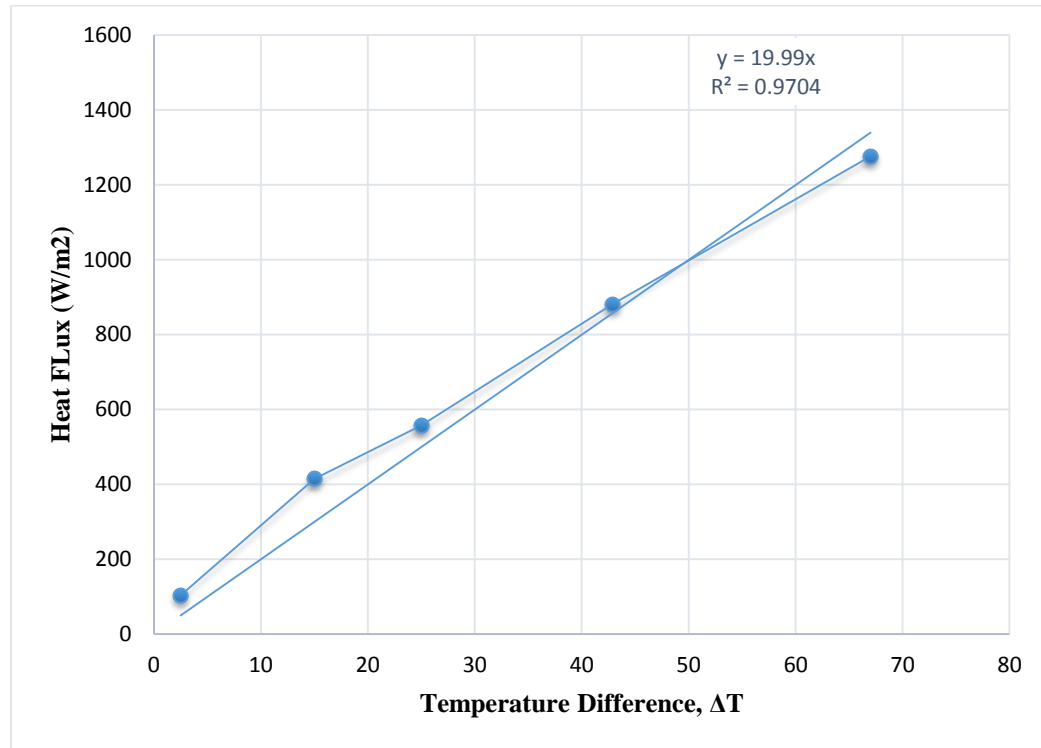


Figure 5-4: Heat leak with increase in temperature

To evaluate heat losses within the channel, the test section was filled with an insulating material without the pins present. For a desired power input, temperatures were

recorded and the heat losses due to the conductivity of the acrylic walls were recorded. Figure 5-4 represents the results of the heat leak test. The total heat flux generated by the heaters is calculated using,

$$q'' = I^2 R \quad (3)$$

The effective heat flux is given by,

$$q''_{eff} = q'' - q''_{loss} \quad (4)$$

The heat transfer coefficient is given by,

$$h = \frac{q''_{eff}}{T_w - T_r} \quad (5)$$

The Nusselt number relation is given by,

$$Nu = \frac{hD}{k} \quad (6)$$

The flow through the channel cooled the heated strips through convection. The aluminum pins also extracted heat from the strips through conduction. Flow rates through the channel were established using a venturi meter. The mass flow rate through the venturi meter was measured by recording the pressure drop across the venturi meter. Reynolds number calculation were based on the pressure drop across the venturi meter.

The Reynolds number through the channel is given by,

$$Re = \frac{\dot{m}D}{\mu A_{eff}} \quad (7)$$

Where,

\dot{m} = Mass flow rate through the venturi meter

D = Pin diameter

μ = Dynamic viscosity of air

A_{eff} = Effective cross sectional area between the pins

5.2 Experimental Data and Analysis

The experimental set up was first validated for a smooth channel case. For the smooth channel case, the pins were removed and experimental Nusselt number profiles were compared against theoretical cases. The experimental data was obtained at a Reynolds number of 25,000 with a heat flux of 950W/m^2 . Figure 5-5 is a representation of the Nusselt number contour of the end wall of the experimental rig.

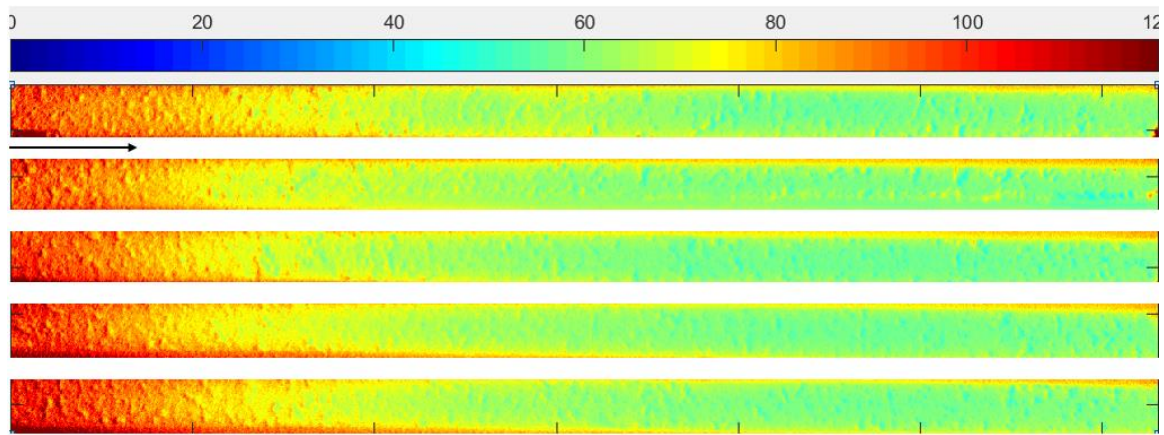


Figure 5-5: Experimental Nusselt number contour

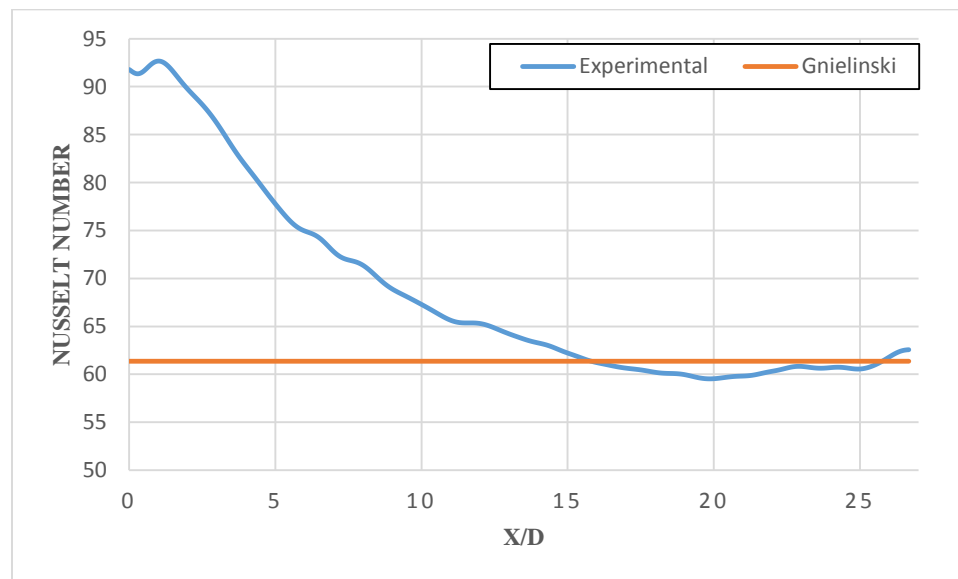


Figure 5-6: Smooth Channel Nusselt number plot

From figure 5-5 it can be seen that as air passes through the smooth channel it starts to cool down the heated section. Maximum cooling is observed in the forward section of the rig. As the flow moves downstream the rate of cooling starts to steady out. Figure 5-6 is a representation of the Nusselt number profile along the rig. The plot compares the Nusselt number profiles obtained experimentally against the theoretical case i.e. Gnielinski correlation. The Gnielinski Nu profile calculations were based on a thermally fully developed fluid flow case and hence show a constant Nusselt number distribution along the rig. For the experimental case the fluid flow is not thermally fully developed as only the test section of the rig was heated. The inlet section used to develop the flow and the outlet section are unheated regions. Figure 5-6 shows that as the flow enters the heated test section it starts to cool it down, eventually reaching a steady state and coming very close to matching the Gnielinski correlation. The experimental case was run at a Reynolds numbers of 10,000 and 15,000 with varying heat flux.

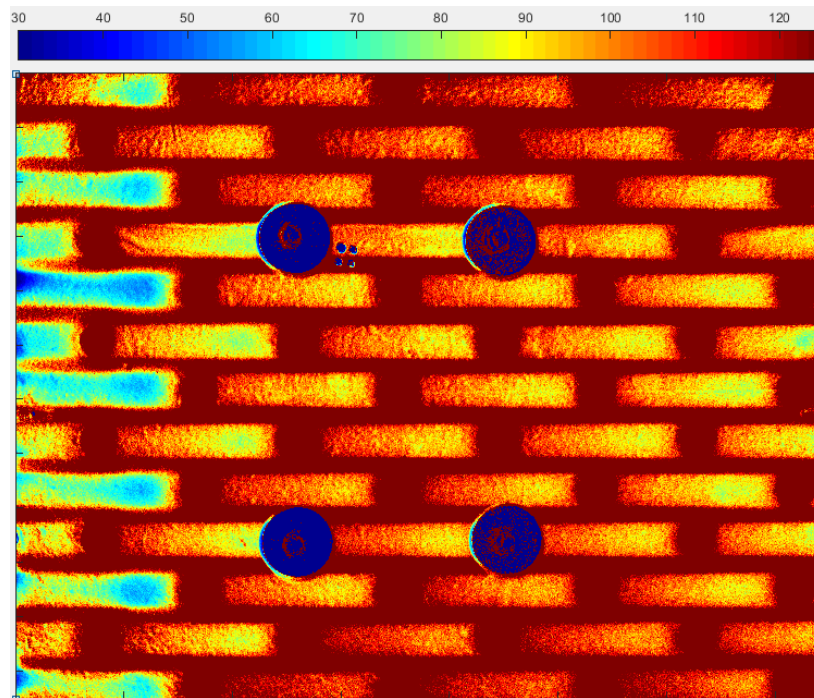


Figure 5-7: Nusselt number contour on experimental test section end wall

Figure 5-7 is a representation of the Nusselt number contour at the end wall of the experimental test section. The dark red circular spaces on the strips represent the locations of the pins resting on the heaters acting as heat conductors. The spacing between the strips is unheated. The 4 washers visible on the image are attached on either side of the end walls passing through the pins, acting as grips to ensure the pins are firmly resting and are in contact with the heated section. Heating the test section caused the end walls to warp, which resulted in a gap between the bottom of the pins and the end wall. It was therefore necessary to use the washers as grips on the end walls pulling them together. For the purpose of this study the 5 strips in the area between the washers were used for data collection.

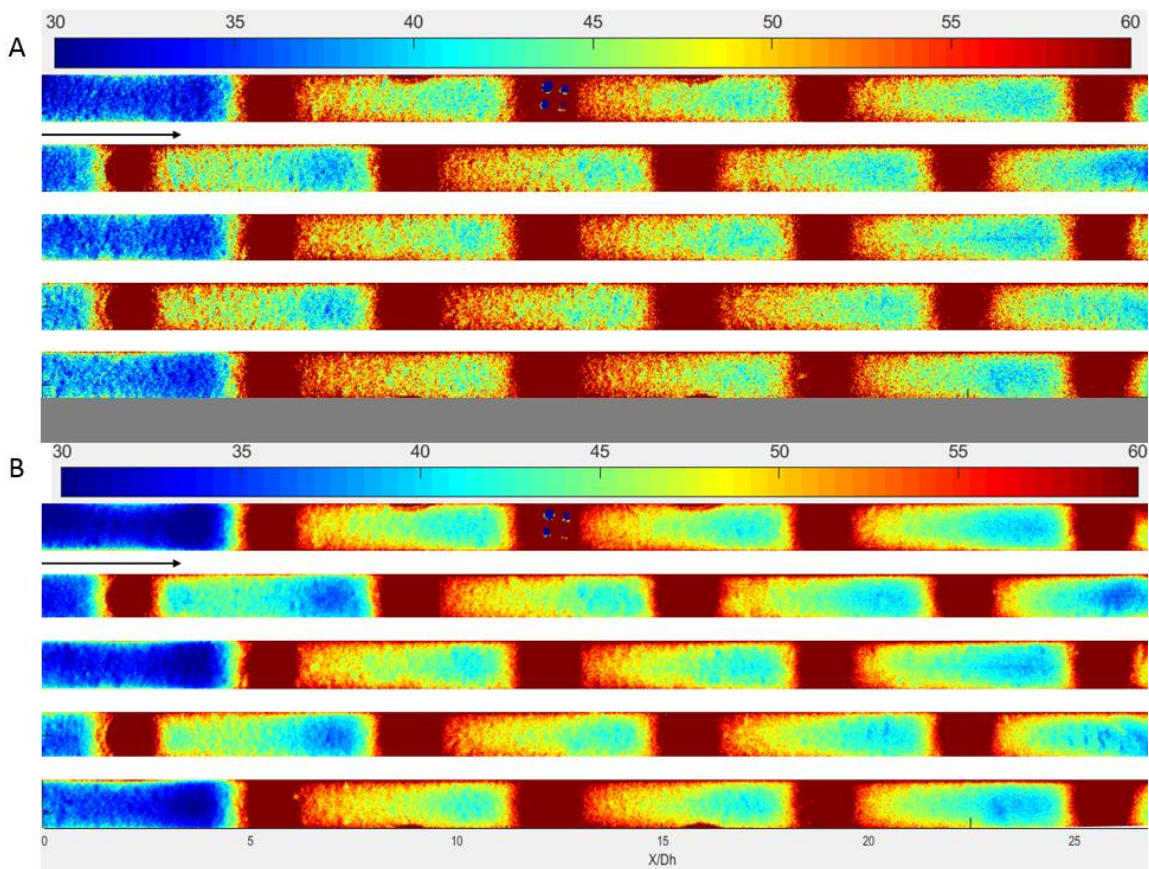


Figure 5-8: Nusselt number contour $Re = 10,000$ A] Heat flux = 450 W/m^2 B] Heat flux = 1200 W/m^2

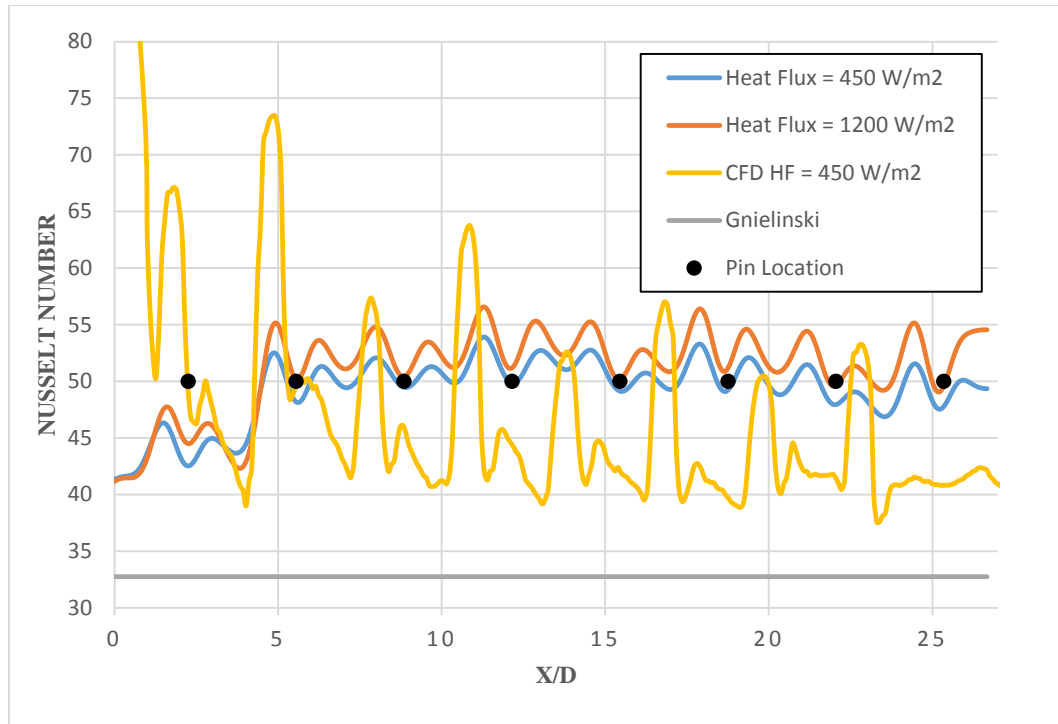


Figure 5-9: Spanwise average Nusselt number $Re = 10,000$

Figure 5-8 is a representation of the Nusselt number contours obtained at a Reynolds number of 10,000. The Nusselt number on the end wall shows that as the flow moves downstream into the array the effective cooling of the end wall increases. Highest end wall temperatures are observed in the region from row one to row three of the array. Behind row three of the array the heat transfer rate tends to steady out.

Figure 5-9 is a plot of span wise average of Nusselt number along the test section at a Reynolds number of 10,000. The plot in figure 5-9 represents Nusselt numbers for two different heat flux cases. The 16 peaks observed on the plot represent the stagnation and wake region of the pins in each of the 8 rows. The first peak represents the stagnation region and the second peak the wake region of the pins in row one of the array. This trend is followed by the subsequent rows of pins downstream.

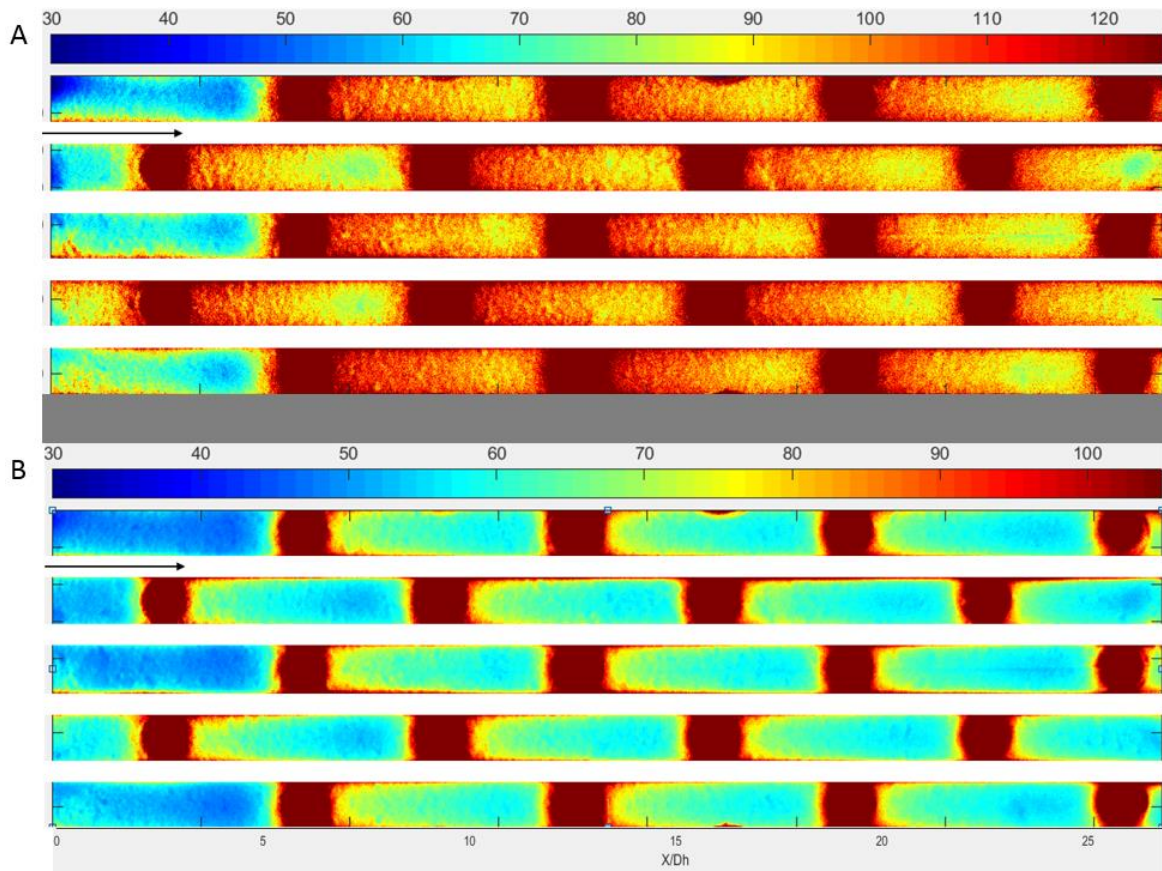


Figure 5-10: Nusselt number contour $Re = 15,000$ A] Heat flux = 1300 W/m^2 B] Heat flux = 3200 W/m^2

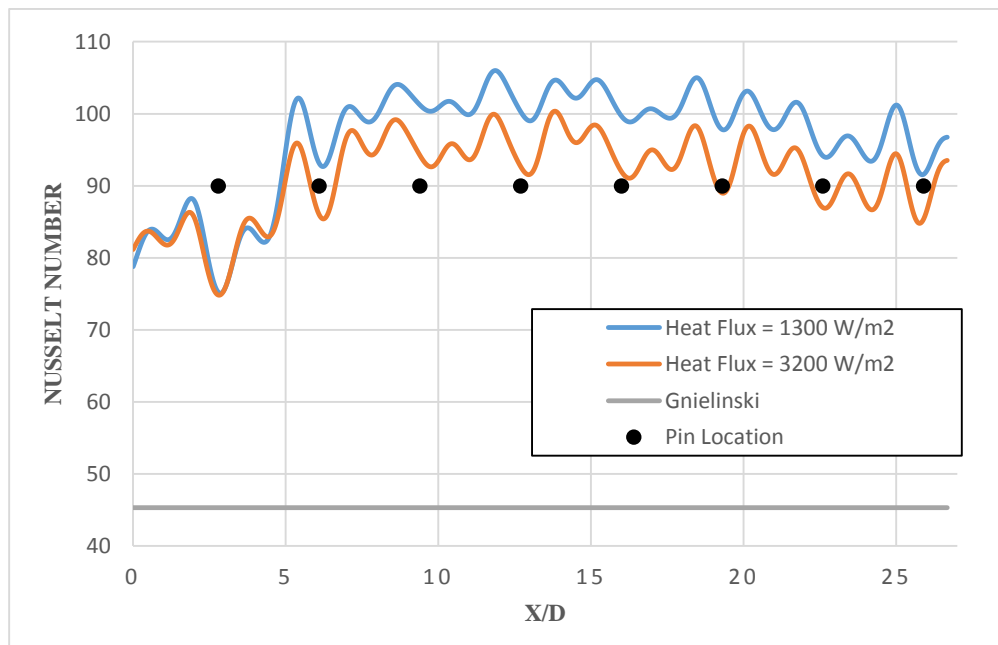


Figure 5-11: Spanwise average of Nusselt number $Re = 15,000$

Figure 5-10 is a representation of the Nusselt number contours at a Reynolds number of 15,000. From figure 5-10 it is observed that at Reynolds number of 15,000, as the heat flux increases the effective cooling of the channel downstream decreases. The Nusselt number plot in figure 5-11 show regions of high cooling at the leading and trailing edge of the pins. These regions are dominated by the effects of wake shedding and turbulent mixing of the mainstream flow that act as drivers of heat transfer. The cool regions at the leading edge of each pin represent the locations of the formation of horseshoe vortices at the end wall. The legs of the horseshoe vortices wrap around the pin at the pin wall junction and break up the wall boundary layer, rolling the cooler fluid towards the heated end wall. The flow in trailing edge region of the pin is dominated by the after effects of the horseshoe vortices and the secondary vortices formed due to adverse pressure gradients and flow separation around the pin. These flow effects cause high shear stress that result in high levels of heat transfer. The temperature contours show that in the region from row one to row three in the array, the levels of heat transfer is fairly constant with a slight increase in the region ahead of the pins in row two. Past the third row a stream wise increase in levels of heat transfer is observed. This indicates that as the flow moves past the third row the turbulent mixing of the flow increases. The high effective cooling due to the turbulent mixing and vortex shedding in the wake regions is observed up to rows five or six. As the flow is fully developed downstream past row six, the temperature distributions observed show a slightly reduced levels of cooling compared to the rows upstream. This indicates that the boundary layer at the end wall begins to thicken up in the region past row six of the array. The trend of increasing levels of heat transfer in the first two or three rows followed by a periodic steadiness was also observed in an experimental study conducted

by Chang et al., (2008). Figure 5-12 is a representation of the end wall Nusselt number profiles of the cases studied by Chang et al., (2008).

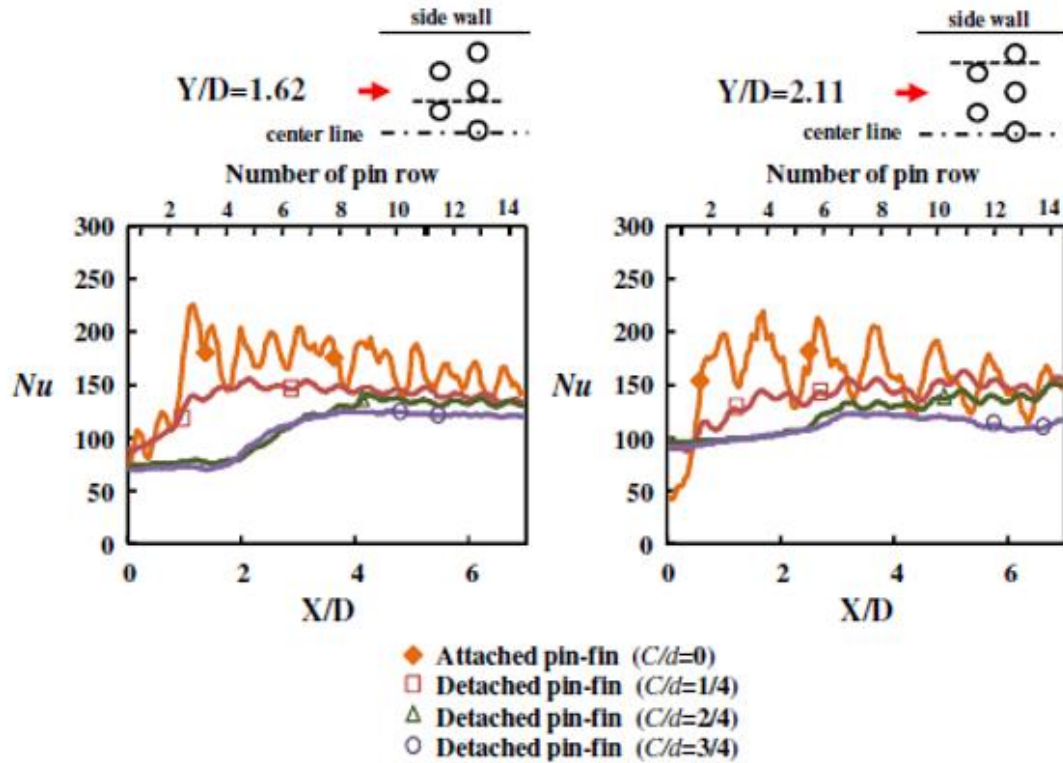


Figure 5-12: Nu Profiles for pin fin channels with $C/d = 0, 1/4, 2/4$, and $3/4$ at $Re = 30,000$ (Chang et al., 2008)

From figure 5-12 we can see that the trend of the end wall Nusselt number distribution matches the trend of the end wall Nusselt number plot obtained in the in-house experimental facility. The Nu profiles for the attached pin fin case show increasing levels of heat transfer moving from the first to the second row regions followed by a periodic steady rate of heat transfer. The high heat transfer rates at the stagnation and wake region of the pins observed in the in-house experimental study is also observed in the Nu profiles in figure 5-12.

Pressure data across the channel was recorded using a U-tube manometer. Pressure taps at the inlet and exit locations of the test section allowed for measuring the pressure gradient across the channel. Pressure drop across the channel was recorded for varying Reynolds numbers.

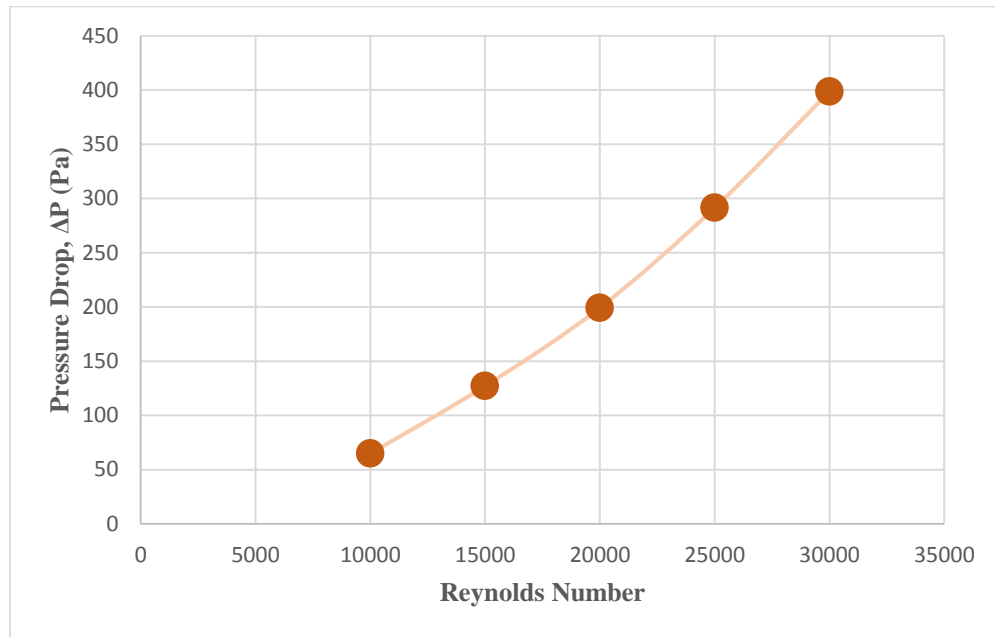


Figure 5-13: Pressure drop across the channel at different Reynolds Numbers

Figure 5-13 is a representation of the pressure drop across the channel at five different Reynolds numbers. The plot shows that as Reynolds number increases, the pressure drop across the channel increases almost linearly. With an increase in Reynolds number the intensity of the turbulence in the channel increases. An increase in turbulence in the channel increases the shear stresses in the channel, which relates to an increase in pressure losses across the channel.

6. Conclusion

The preceding study examined the flow characteristics of pin fin channels. A benchmarking study was conducted to verify the accuracy of the flow physics of some of the RANS turbulence models used in the industry for computational fluid dynamics simulations. The study showed that the accuracy of matching of the turbulence models depended on the location in the array and on the Reynolds number. Comparisons of the three turbulence models used in the study showed that at the first row i.e. forward section of the channel, the QRK-E and KO-SST models predicted heat transfer most accurately for the low Reynolds number cases. At high Reynolds numbers at row 1, on averaging, the KO-SST model predicted heat transfer levels closest to that of experimental values. As the flow moves down into the array, the quality of the turbulence models matching experimental data tends to change. At row 5 in the array, the QRK-E model tends to predict the trend of the experimental data closest at low and high Reynolds numbers. The KO-SST model struggles to accurately predict stagnation point heat transfer down the array. Although the trend of the data from the KO-SST models does not match the experimental data, averaging the circumferential values shows a close match to the experimental data. Overall, for heat transfer profiles, all the turbulence model seem to match well near the stagnation point and along the favorable pressure gradient region except for the highest Reynolds number cases and in the regions of adverse pressure gradients. Basic RANS turbulence models seem to struggle at high Reynolds numbers and in regions of adverse turbulence.

At row 5 of the pin fin array all three turbulence models were found to closely match pressure coefficients at low Reynolds number, and under predict at high Reynolds

numbers. At high Reynolds numbers all three turbulence models do a good job at capturing stagnation point pressure coefficients but over predict pressure losses in the wake region of the pin. On averaging the data, the QRK-E model matched experimental data the closest. The difference between experimental values and CFD predictions for pressure coefficients at high Reynolds numbers is quite large, suggesting further work and study of other available turbulence models is necessary before an overall best match can be determined.

The aim of the biomimicry study was to investigate the flow features involved with complex pin geometries in order to improve on the rates of heat transfer and reduce the adverse pressure losses accompanying a fin cooling channel. The seal whisker geometry chosen showed overall improvements in channel performance when compared to a standard cylindrical pin fin. Elliptic and circular pins treated with the undulations were compared to that of a circular pin fin. The elliptic bio pin showed the most improvement in pressure drop across the channel with a 50% improvement in performance. However, the elliptic pin showed an 11% averaged decrease in heat transfer across the channel. The cylindrical bio pin showed an overall better performance compared to that of the elliptic pin, as it satisfied the criteria of improved heat transfer rates along with reduced pressure drops across the channel when compared to the cylindrical pin fin. The cylindrical bio showed a 2% increase in heat transfer rate accompanied with a 41% decrease in pressure drop across the channel. Overall, the cylindrical pin treated with the undulations observed on seal whiskers shows an improvement worth noticing over a standard cylindrical pin fin.

Results obtained from the experimental set up showed Nusselt number distributions at the end wall for different Reynolds number and heat flux cases. The trend of the Nusselt number profiles at the end wall matched experimental cases from various literature sources.

7. Recommendations

This study helped to understand the flow physics involved with a pin fin channel to study the effects of heat transfer and pressure drop across the channel. A preliminary investigation of complex pin geometries was also conducted to improve on the heat transfer levels and reduce pressure drop. The next step would be to conduct a study to understand the physics of the flow features due to the undulations on the bio pin surface. Further studies could also investigate the effects of changing the amplitude and spacing of the undulations on heat transfer and pressure loss characteristics.

The next step would be to continue research on the conduction effects of the pins on end wall heat transfer. The experimental rig was set-up to study the effects of end wall heat transfer due to convection and conduction. Due to time constraints current study accounted for end wall heat transfer due to convection while ignoring the effects of conduction.

The experimental set up could also be used to study the effects of the flow features on heat transfer, due to the undulations on the biomimicry pins. The set-up will require 3D printing of the bio pins.

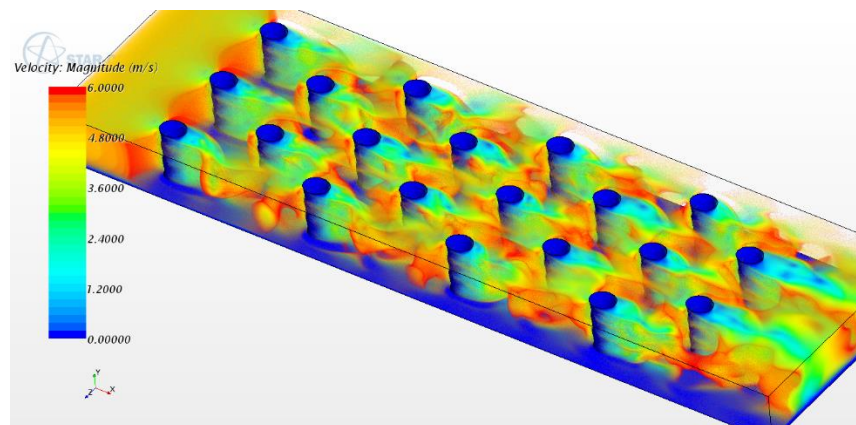


Figure 7-1: Cylindrical bio pin channel velocity contour

8. Publications Resulting from Current Study

Fernandes, R., Ricklick, M., & Pai, Y. (2015). CFD Benchmarking of Heat Transfer and Pressure Drop Predictions in a Pin Fin Channel. In *51st AIAA/SAE/ASEE Joint Propulsion Conference* (p. 3736).

REFERENCES

- Ames, F. E., Dvorak, L. A., & Morrow, M. J. (2004, January). Turbulent augmentation of internal convection over pins in staggered pin fin arrays. In *ASME Turbo Expo 2004: Power for Land, Sea, and Air* (pp. 787-796). American Society of Mechanical Engineers.
- Ames, F. E., & Dvorak, L. A. (2006, January). The influence of reynolds number and row position on surface pressure distributions in staggered pin fin arrays. In *ASME Turbo Expo 2006: Power for Land, Sea, and Air* (pp. 149-159). American Society of Mechanical Engineers.
- Ames, F. E., & Dvorak, L. A. (2006). Turbulent transport in pin fin arrays: experimental data and predictions. *Journal of turbomachinery*, 128(1), 71-81.
- Brigham, B. A., & Van Fossen, G. J. (1984). Length to diameter ratio and row number effects in short pin fin heat transfer. *ASME, Transactions, Journal of Engineering for Gas Turbines and Power* (ISSN 0022-0825), 106, 241-245.
- Chang, S. W., Yang, T. L., Huang, C. C., & Chiang, K. F. (2008). Endwall heat transfer and pressure drop in rectangular channels with attached and detached circular pin-fin array. *International Journal of Heat and Mass Transfer*, 51(21), 5247-5259.
- Chyu, M. K., Hsing, Y. C., Shih, T. P., & Natarajan, V. (1999). Heat transfer contributions of pins and endwall in pin-fin arrays: effects of thermal boundary condition modeling. *Journal of Turbomachinery*, 121(2), 257-263.
- GE Global Research | Ceramic Matrix Composites. (n.d.). Retrieved March 24, 2016, from <http://www.geglobalresearch.com/innovation/ceramic-matrix-composites-improve-engine-efficiency>
- Han, J. C. (2004). Recent studies in turbine blade cooling. *International Journal of Rotating Machinery*, 10(6), 443-457.
- Han, J. C., Dutta, S., & Ekkad, S. (2012). *Gas turbine heat transfer and cooling technology*. CRC Press.
- Hanke, W., Witte, M., Miersch, L., Brede, M., Oeffner, J., Michael, M., & Dehnhardt, G. (2010). Harbor seal vibrissa morphology suppresses vortex-induced vibrations. *The Journal of experimental biology*, 213(15), 2665-2672.
- Hwang, J. J., & Lui, C. C. (2002). Measurement of endwall heat transfer and pressure drop in a pin-fin wedge duct. *International Journal of Heat and Mass Transfer*, 45(4), 877-889.

- Lei, Z. (2005). Effect of RANS turbulence models on computation of vortical flow over wing-body configuration. *Transactions of the Japan Society for Aeronautical and Space Sciences*, 48(161), 152-160.
- Meher-Homji, C. B., Zachary, J., & Bromley, A. F. (2010, October). Gas Turbine Fuels-System Design, Combustion and Operability. In *Proceedings of the 39th Turbomachinery Symposium, George R. Brown Convention Center, Houston, Texas* (pp. 4-7).
- Metzger, D. E., & Haley, S. W. (1982, April). Heat transfer experiments and flow visualization for arrays of short pin fins. In *ASME 1982 International Gas Turbine Conference and Exhibit* (pp. V004T09A007-V004T09A007). American Society of Mechanical Engineers.
- Morris, W. D., & Chang, S. W. (1997). An experimental study of heat transfer in a simulated turbine blade cooling passage. *International Journal of Heat and Mass Transfer*, 40(15), 3703-3716.
- Peles, Y., Koşar, A., Mishra, C., Kuo, C. J., & Schneider, B. (2005). Forced convective heat transfer across a pin fin micro heat sink. *International Journal of Heat and Mass Transfer*, 48(17), 3615-3627.
- Ricklick, M. A., & Carpenter, C. (2014). Comparison of Heat Transfer Prediction for Various Turbulence Models in a Pin Fin Channel.
- Sahiti, N., Lemouedda, A., Stojkovic, D., Durst, F., & Franz, E. (2006). Performance comparison of pin fin in-duct flow arrays with various pin cross-sections. *Applied Thermal Engineering*, 26(11), 1176-1192.
- Shyam, V., Ameri, A., Poinsatte, P., Thurman, D., Wroblewski, A., & Snyder, C. (2015, June). Application of Pinniped Vibrissae to Aeropropulsion. In *ASME Turbo Expo 2015: Turbine Technical Conference and Exposition* (pp. V02AT38A023-V02AT38A023). American Society of Mechanical Engineers.
- Uzol, O., & Camci, C. (2005). Heat transfer, pressure loss and flow field measurements downstream of staggered two-row circular and elliptical pin fin arrays. *Journal of heat transfer*, 127(5), 458-471.
- Wadley Research Group, (2013). High Temperature Coatings. (n.d.). Retrieved January 26, 2016, from <http://www.virginia.edu/ms/research/wadley/high-temp.html>
- VanFossen, G. J. (1982). Heat-transfer coefficients for staggered arrays of short pin fins. *Journal of Engineering for Power*, 104(2), 268-2

